Methane transport and sources in an Arctic deep-water cold seep offshore NW Svalbard (Vestnesa Ridge, 79°N)

Simone Sauer[1]*, Wei-Li Hong[2], Haoyi Yao[1], Aivo Lepland[2], Martin Klug[2], Florian Eichinger[3], Tobias Himmler[2], Antoine Crémiere[4], Giuliana Panieri[1], Carsten J. Schubert[5], Jochen Knies[2]

[1]CAGE – Centre for Arctic Gas Hydrate, Environment and Climate, UiT-The Arctic University of Norway, Department of Geosciences, 9037 Tromsø, Norway
[2]Geological Survey of Norway, 7491 Trondheim, Norway
[3]Hydroisotop GmbH, Schweitenkirschen, Germany
[4]Division of Geological and Planetary Sciences, California Institute of Technology, Pasadena, California, USA
[5]EAWAG, Swiss Federal Institute of Aquatic Science and Technology, Kastanienbaum, Switzerland
*current affiliation : IUEM-Institut Universitaire Européen de la Mer, LEMAR, Rue Dumont d'Urville, 29280 Plouzané, France.

Abstract.

We investigate the uppermost 60 cm of sediment in active pockmarks of a deep-water methane seep site from Vestnesa Ridge offshore NW Svalbard. Using video guided core sampling with a remotely operated vehicle we collected push cores directly from bacterial mats within two active pockmarks, Lunde and Lomvi. Pore water analyses show very shallow sulphate methane transition zones and transport-reaction modelling suggests a considerable amount of dissolved methane passing through the sediment water interface due to upwards advection of an aqueous fluid not previously reported from Vestnesa Ridge. In addition, we show that the amount of methane that bypasses the benthic methane filter greatly increases with higher aqueous fluid advection rate. Recent changes in methane flux are evident from lipid biomarker, seep carbonate, and δ^{13}C-organic carbon profiles in both pockmarks. Hydrocarbons at this cold seep site are supplied both by deep thermogenic sources from below the gas hydrate stability zone but also to a significant degree by microbial methanogenesis which dominates the signature in our shallow sediment cores with $\delta^{13}C\text{-}CH_4$ values as low as -77‰.

Keywords: methane, aqueous fluid advection, pore water modeling, microbial methanogenesis, Arctic cold seep

1 Introduction

The Arctic is vulnerable to ongoing climate change and potential release of currently trapped geological methane in gas hydrates, which might eventually affect the future atmospheric methane concentration (IPCC, 2019). However, current knowledge states that seafloor methane release has no significant influence on the atmospheric methane concentrations (e.g. Ferré et al., 2020; Myhre et al., 2016) and that anthropogenic climate change is not yet enhancing gas-hydrate destabilization (Hong et al., 2017; Wallmann et al., 2018). Studies have focused mostly on shallow water seep sites (<400 m) including western Svalbard (Prins Karls Forland) (Jansson et al., 2019; Myhre et al., 2016; Silyakova et al., 2020), the East Siberian Arctic shelf (Puglini et al., 2019; Shakhova et

al., 2010) and the Barents Sea Shelf (e.g. Storfjordrenna, Andreassen et al., 2017; Hong et al., 2017). In contrast, seep dynamics from deep-water gas reservoirs are largely unconstrained, except for the Vestnesa Ridge gas hydrate system offshore NW Svalbard. Here, numerous studies have investigated the controlling factors for active methane release from seafloor pockmarks (Knies et al., 2018; Panieri et al., 2017; Plaza-Faverola et al., 2015; Schneider et al., 2018; Vogt et al., 1994; Westbrook et al., 2009). Changes in the stress regime due to glacial forebuldge propagation influencing fault activation and permeability (Himmler et al., 2019; Plaza-Faverola and Keiding, 2019) have been suggested as factors influencing methane seepage in the past. These constraints on past methane seepage at Vestnesa Ridge are derived from (1) studying paleo-pockmarks in the seismic record (Plaza-Faverola et al., 2015), (2) dating of seep carbonates (Himmler et al., 2019), (3) analysing overgrowth of secondary carbonates on benthic and planktonic foraminifera (Panieri et al., 2016; Schneider et al., 2018) and (4) dating bivalve shell beds with ^{13}C-depleted signatures which feed on chemosynthetic bacteria (Ambrose et al., 2015). Buried pockmarks and gas chimneys mapped at several stratigraphic intervals in seismic profiles suggest episodic seepage activity starting at approximately 2.7 Ma (Plaza-Faverola et al., 2015). Seep carbonate dating suggests that episodic methane seepage in pockmarks on the eastern segment of Vestnesa Ridge has been ongoing since at least the penultimate glacial maximum ~160 ka ago (Himmler et al., 2019). The controlling factor of the present-day seepage pattern, however, is thought to be the orientation of faults in relation to the stress field caused by the nearby ultra-slow mid-ocean ridge spreading (Plaza-Faverola and Keiding, 2019).

Numerous studies have investigated gas composition of dissolved methane in the sediment pore water and also in gas hydrate samples (Graves et al., 2017; Panieri et al., 2017; Plaza-Faverola et al., 2017; Smith et al., 2014). However, a limited dataset has hindered reliable conclusions on gas sources in different sediment depths and transformation processes until recently, also because dissolved methane sampled by the headspace method can have undergone intensive biogeochemical modifications already. In a study by Pape et al. (2020) the investigation of gravity cores and MeBo cores from the active Lunde pockmark on Vestnesa Ridge down to a depth of 62 mbsf sheds light on the origin of light hydrocarbons in gas hydrate and sediments on Vestnesa Ridge. The authors find that deep thermogenic hydrocarbons migrate upwards from a depth of more than 800 m and dominate the gas in gas hydrates. Evidence for microbial methanogenesis is found mostly in samples from depths shallower than 50 mbsf suggesting that microbial methane contribution is more important at Vestnesa Ridge than previously thought. However, at higher methane flux sites the signature of microbial methane is mostly overprinted by deeper thermogenic methane.

While studies show the importance of gas migration, the significance of aqueous fluid advection and its impact on local carbon cycling is less emphasized. Hong et al. (2018) showed that aqueous fluid advection could dominate the fluid system once the free gas supply has terminated. Previous studies have investigated how the amount of methane escaping the seafloor varies as a function on fluid flow velocity or different permeabilities (Luff et al., 2004; Stranne et al., 2019; Wallmann et al., 2006), but this has not been investigated at Vestnsea Ridge yet.

Here we present pore fluid and sediment geochemistry data from shallow (down to 60 cmbsf) push cores sampled from two active pockmarks using a video guided remotely operated vehicle (ROV). We sampled cores directly from locations that exhibit gas discharge features allowing to study the fluid flow regime (i.e. diffusive or advective), and its influence on carbon cycling and the efficiency of the benthic methane filter, using reaction-transport modelling. Furthermore, we investigate the gas composition (thermogenic vs microbial) of the dissolved gas in the sediment pore water, and also the relationship of carbon isotopes between the different reservoirs of the cold seep system: methane, dissolved inorganic carbon, sedimentary organic matter and seep carbonate nodules, and assess biogeochemical processes occurring in seep-dominated marine sediments.

2 Geological Setting

Vestnesa Ridge is a submarine, elongated, c. 100 km long sediment drift located offshore NW Svalbard with an extensive gas hydrate and free gas system (Fig. 1). Vestnesa Ridge lies to the east of the slow-spreading Molloy Ridge, and to the north of the Molloy fracture zone (Hustoft et al., 2009). The sediment succession is several kilometres thick and subdivided into three seismo-stratigraphic sequences (Eiken and Hinz, 1993). The topmost sediments on the ridge crest are late Weichselian and Holocene deposits composed of silty turbidites and muddy-silty contourites (Howe et al., 2008). Gas hydrates and seabed fluid flow systems are widespread along continental margins (Judd and Hovland, 2007) but Vestnesa Ridge is a unique setting in that it is situated close to a mid-ocean spreading centre and thus is underlain by relatively young and hot oceanic crust with a heat flux of more than 115 mW/m^2 (e.g. Engen et al., 2008; Hustoft et al., 2009). Vestnesa Ridge bends from an E-W direction to a SE-NW direction, and an elongated pockmark field with more than 100 individual pockmarks up to 600 m in diameter are aligned along the crest (Hustoft et al., 2009; Vogt et al., 1994) (Fig. 1). On the western segment pockmarks are scattered on a larger area of the ridge, whereas on the eastern segment they align almost perfectly on the narrow ridge crest. Only the eastern segment has shown periodic active gas discharge in recent years (Bünz et al., 2012).

The bottom-simulating-reflector (BSR) is located at approximately 200 mbsf (Hustoft et al., 2009). Below the BSR, a free gas layer of approximately 30-100 m thickness was inferred (Bünz et al., 2012; Goswami et al., 2015; Hustoft et al., 2009). The topography of Vestnesa Ridge and the prominent BSR anticline below the ridge crest control the gas accumulation. Seismic chimneys, which pierce the complete gas hydrate stability zone (GHSZ), are believed to be the gas migration pathways that supply gas to the seafloor and created the pockmarks (Bünz et al., 2012).

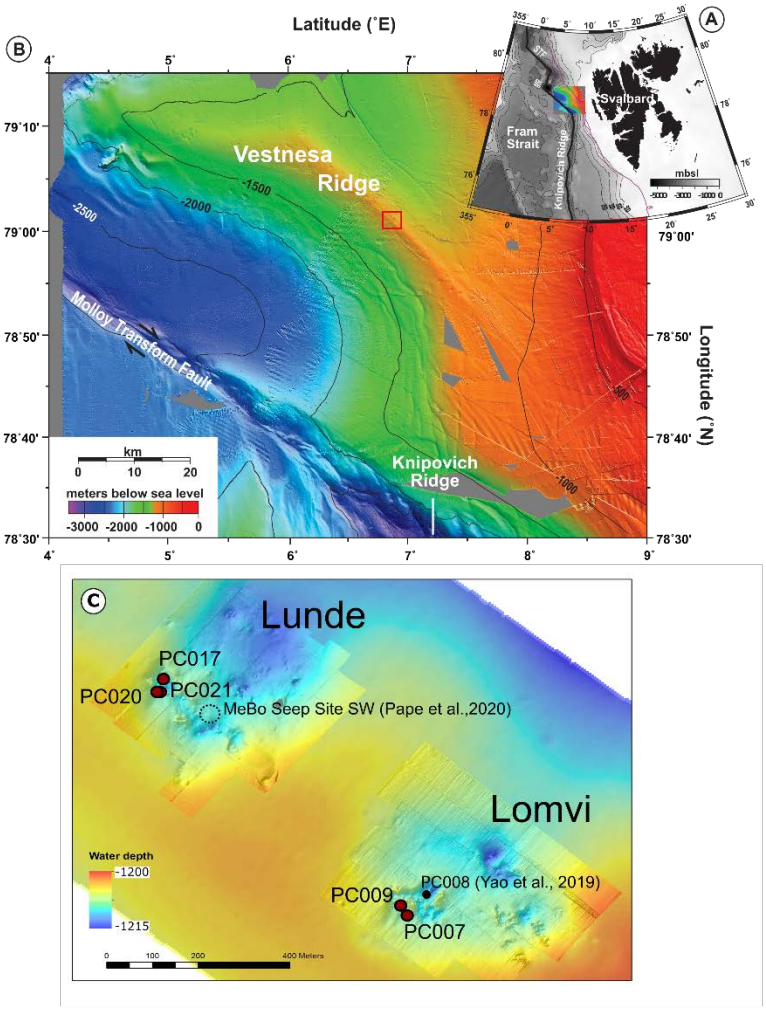

Figure 1:A) Overview map of Svalbard and the Fram Strait. B) Bathymetry of the NW Svalbard margin modified from (Schneider et al., 2018). Bathymetry data from (Jakobsson et al., 2012). The red square on Vestnesa Ridge is the approximate location of the pockmarks Lunde and Lomvi. C) ROV-obtained high resolution bathymetry of the pockmarks Lunde and Lomvi with push core locations indicated as red dots and black dots (PC008 from Yao et al.,2019). The dotted circle indicates the area of MeBo Seep site SW investigated by (Pape et al., 2020).

3 Study Area

3.1 Lunde and Lomvi pockmarks

Two of the most active pockmarks in the eastern segment of Vestnesa Ridge are the Lomvi and Lunde pockmarks (Panieri et al., 2017). Seafloor images of these two pockmarks reveal authigenic seep carbonates and extensive chemosynthetic communities (Himmler et al., 2019; Panieri et al., 2017). The two pockmarks show complex internal bathymetry comprising depressions and ridges (Fig. 1C). 3D seismic data revealed a vertical acoustic chimney structure beneath Lund and Lomvi which extends from the base of the hydrate stability zone up to the seafloor (Bünz et al., 2012). Reflection anomalies beneath the two pockmarks indicate upward advection of free gas and some enhanced reflections could be the result of gas hydrate and/or seep carbonate horizons in the subseafloor (Himmler et al., 2019; Panieri et al., 2017).

4 Sample collection

On research vessel "G.O. Sars" expedition P1606 to the Vestnesa Ridge in July 2016 we collected five push cores (PC007, PC009, PC017, PC020 and PC021) using ROV Ægir 6000. Using video guidance, we chose sites close to bacterial mats and exposed seep carbonates in both pockmarks to collect the push cores (Fig. 2, Table 1). One push core (PC020) was collected in a location without any signs of seepage (Table 1). Several push cores were retrieved during a single ROV dive and stored in a basket at the seafloor until the end of the ROV dive. Immediately upon recovery of the basket the push cores were sampled for pore water using the rhizon technique and for gas using the headspace technique. Headspace gas was sampled using cut off 5 ml syringes and extracting exactly 3 ml of sediment through pre-drilled holes in the liner. The sediment was transferred to serum glass vials containing a 2.5% NaOH solution. They were then crimp sealed and stored at 4ºC. Pore water was extracted using 5 cm rhizon samplers (Rizosphere, Netherlands) (Seeberg-Elverfeldt et al., 2005), which were inserted through pre-drilled holes at intervals ranging from 2 cm to 6 cm. Pore water was collected in 10 ml acid-washed syringes. Pore water splits were prepared for alkalinity and dissolved Fe^{2+} analyses onboard, and for anion, cation (1vol% HNO_3) and $\delta^{13}C$-DIC analyses and nutrient (frozen) analyses in onshore laboratories. After offshore sampling, the push cores were frozen onboard and kept at -18°C until further processing.

Table 1:Push core locations, water depth, core length and basic seafloor description of the sampling site. We differentiate between black sediment patches (often the precursor of bacterial mats) and white sulfur-oxidising bacterial mats (e.g. Treude et al., 2009)

Core	Pockmark	Latitude (°N)	Longitude (°E)	Water Depth (m)	Core length (cm)	Seafloor Observations
PC020 (non-seep)	Lunde	79.0075	6.8990	1206.7	72	Muddy brown sediment

PC017	Lunde	79.0078	6.8994	1205.0	51	Muddy sediment with black sediment patches
PC021	Lunde	79.0075	6.8989	1206.5	39	Muddy sediment with black sediment patches and some white sulfur-oxidising bacterial mats. Core taken between black sediment patches.
PC007	Lomvi	79.0023	6.9225	1204.0	38	Core from medium-sized white bacterial mat
PC009	Lomvi	79. 0025	6.9220	1205.1	27	Area of white bacterial mat (with smaller black sediment patches) among dark brown silty clay, surrounded by seep carbonate crusts; core taken inside white bacterial mat.

134

135 **5 Methods**

136 **5.1 Porewater analyses**

137 Total alkalinity (TA) was determined with a pH-controlled titration to a pH just under 4 with an HCl titrant (12M
138 Sigma-Aldrich TraceSELECT HCl diluted to 0.012M). The pH electrode was calibrated against pH 4, 7 and 10
139 Metrohm Instrument buffers. We titrated 0.1 to 1 ml of sample aliquot depending on the amount of pore water
140 recovered. About 10 ml of 0.7M KCl was added to each sample to ensure that the pH electrode was fully
141 submerged. Titrant acid was added while constantly stirring in an open 50 ml beaker. The amount of acid and pH
142 was manually recorded during each addition. TA was calculated from the Gran function plots, which were made
143 by plotting Gran functions against the titrant volume. Gran function is defined as:

144 $(V_0+V_t)*10\text{-pH}$, where V_0 is the initial volume of sample and V_t is the volume of titrant added. The TA was then
145 estimated from the slope and intercept of the regression line from the Gran function plot. Six to ten points were
146 used for regression. All titrations were done less than six hours after the syringe disconnected from the rhizons.
147 Dissolved iron (Fe^{2+}) was determined photometrically using a Shimadzu UVmini-1240 UV-Vis
148 Spectrophotometer at a wavelength of 565 nm. Addition of a commercial ferrospectral solution (prepared
149 onboard with O_2-free MiliQ water) to the pore water samples causes the formation of a violet colour complex
150 (Collins et al., 1959). The UV absorption at 565 nm is proportional to the concentration of dissolved iron in the
151 sample (Beer-Lambert law). Calibration was performed using five standards of known Fe^{2+} concentration up to
152 1.5 ppm. If samples had higher Fe^{2+} concentration than 1.5 ppm they were diluted with O_2-free ascorbic acid
153 solution. For sulphate (SO_4^{2-}) analyses, we used a Dionex ICS – 1100 Ion Chromatograph with an AS-DV
154 autosampler and an IonPac AS23 column (eluent: 4.5 mM Na2CO3/0.8 mM NaHCO3, flow: 1ml/min) at the
155 Geological Survey of Norway. The relative standard deviations from repeated measurements of different

laboratory standards are better than 0.5% for concentrations above 0.1 mM. Cation concentrations were determined by inductively coupled plasma atomic emission spectroscopy (ICP- AES) at the Geological Survey of Norway using a Perkin Elmer Optima 4300 Dual View. Samples were diluted 1:40 before analysis.

Methane (CH_4) concentration in the sediment was analysed by equilibrium partitioning and measured at the Swiss Federal Institute of Aquatic Science and Technology (EAWAG) using an Agilent Gas Chromatograph G1530N with a flame ionization detector. The relative standard deviation of the CH_4 measurements based on repeated measurements of a calibration standard was ± 2.9%. The CH_4 concentration was calculated by adding the headspace CH_4 concentration to the CH_4 concentration in the fluid/sediment which was calculated using the Bunsen coefficients from Yamamoto et al. (1976) taking into account temperature and salinity. Assuming a constant porosity of 0.7 we calculated the CH_4 concentration in the pore water. The porosity value was estimated from porosity data from core JR211-26 from Vestnesa Ridge (Hong et al., 2016). Due to potential degassing during core recovery, the measured methane concentrations are always regarded as a minimum value. The isotopic composition of DIC in pore water (δ^{13}C-DIC) was determined on the CO_2 liberated from the water after acidification with phosphoric acid. Measurements were performed at EAWAG using an IRMS (Isotope Ratio Mass Spectrometer) from Micromass (Isoprime) equipped with a Gilson 222XL Liquid Handler and a Multiflow from Isoprime. The standard deviation of the δ^{13}C-DIC measurements from repeated measurements of a standard was ±0.12‰ (1σ, n=52). The stable carbon isotope values for DIC are reported in the conventional δ notation in permil (‰) relative to V-PDB (Vienna Pee Dee Belemnite). Concentrations of phosphate and ammonium were determined colorimetrically with a Technicon AutoAnalyzer II™ component at Oregon State University. Details of the analyses have been documented in the United States Environmental Protection Agency (US EPA) Criteria "EPA 600/4-79-020 Methods for Chemical Analysis of Water and Wastes" and can be found online (EPA, 1983). The stable carbon isotopes of methane (δ^{13}C-CH_4) and ethane (δ^{13}C-C_2H_6) and hydrogen isotopes of methane (δ^{2}H-CH_4) were analysed at Hydroisotop GmbH, Germany, using a GC-MS-IRMS system (Thermo Fisher Scientific GmbH) (for details see Sauer et al. (2015)). The isotopic composition is reported in ‰ (δ-values) against the international standards VPDB for carbon and Vienna Standard Mean Ocean Water (VSMOW) for hydrogen.

5.2 Sediment geochemistry

Core images, X-Ray fluorescence (XRF) and magnetic susceptibility (MS) logging

184 The sediment cores were analysed at the NGU core logging facilities in Trondheim, Norway. In the laboratory
185 the frozen cores were split lengthwise using a bandsaw and a diamond equipped blade. After thawing, the
186 surfaces were cleaned to remove any smeared sediment and to prepare for imaging. High-resolution images were
187 taken using a GeoScan IV colour line-scan camera with an AF Nikkor 50 mm f/1.8D lens mounted to a Standard
188 MSCL (MSCL-S) core logger (GeoTek Ltd., UK). After imaging the core surface was covered with a 4 µm
189 Ultralene film (Spex Sample Prep, USA) to avoid cross-contamination and XRF and MS measurements were
190 taken incrementally at 0.5~cm resolution along the longest axis in the centre of the core surfaces. XRF down
191 core logging was carried out with a Delta Innov-X portable XRF sensor (Olympus NDT Inc., USA) attached to
192 the MSCL-S core logger. The pXRF sensor is equipped with a 4W Rh Tube anode and Si drift detector. Prior to
193 core measurements the pXRF sensor was standardized and a customised standard sample was stationary
194 measured for sensor-control purposes. Successive measurements with voltage settings between 50 and 15 keV
195 voltage and 20 sec exposure time provided spectra covering chemical elements from Mg to Pb. The spectra were
196 converted to element concentration in ppm using the Compton normalization approach described elsewhere (e.g.
197 Kenna et al., 2011). From the element spectrum measured the ratio of calcium (Ca) to titanium (Ti)
198 concentrations were used for this study. MS was measured using a MS2E sensor and a MS3 (both Bartington
199 Instruments Limited, UK) attached to the MSCL-S core logger with 10 sec exposure time at the same sample
200 depths as in XRF measurements. Results are reported in 10^{-5}SI units.

201 Sediment samples were taken after core scanning at a resolution of ~2.5 cm for the analyses of carbon and
202 nitrogen content and δ^{13}C-TOC. Carbonate nodules were found exclusively in PC009 and sampled for
203 determination of mineral composition by XRD and δ^{13}C analyses.

204 Carbon and nitrogen content (LECO)

205 All sediment samples were freeze-dried, ground and homogenized at the Geological Survey of Norway. Total
206 carbon (TC) and total organic carbon (TOC) content of the sediment samples were analysed using a LECO SC-
207 632. For TC determination, subsamples of 300-400 mg were combusted at 1350˚C while measuring the
208 production of CO_2. For TOC analyses, subsamples of 400-500 mg were pre-treated with 10 vol% HCl to remove
209 inorganic carbon and then rinsed with MilliQ water. Subsequently they were analysed in the same way as
210 described for TC. Total inorganic carbon (TIC) was then calculated as TIC = TC – TOC. All results are given in
211 weight percent (wt%) and the standard deviation for the TC and TOC measurements was ± 0.06 wt%. The lower
212 limit of detection was 0.06 wt% and 0.1 wt% for TC and TOC, respectively. Total nitrogen (TN) analyses were
213 performed with a LECO FP 628 Nitrogen Determinator. Subsamples of 200 mg, wrapped in tin foil, were

combusted to NOx, which was transformed to N_2 and detected with a thermal conductivity cell. The standard deviation of the measurement was ±0.01wt% and the lower limit of detection was 0.1 wt%. The ratio of organic carbon over nitrogen content (hereafter C_{org}/N_{tot} ratio) was calculated by dividing the wt% values and the multiplying by 1.167 to obtain the atomic ratio.

The carbon isotopic composition of sedimentary organic matter ($\delta^{13}C$ – TOC) was analysed by EA-IRMS (Elemental Analyzer Isotope Ratio Mass Spectrometry) at Iso Analytical Ltd, UK. Subsampled were decarbonated with 10vol% HCl prior to analyses with a RoboPrep-CN elemental analyzer coupled to a Europa Scientific 20-20 IRMS. Reference materials used for quality control were: reference standard IA-R001 (wheat flour, $\delta^{13}C$: -26.43‰ V-PDB), reference standards IA-R005 (beet sugar, $\delta^{13}C$: -26.03‰ V-PDB) and reference standard IA-R006 (cane sugar, $\delta^{13}C$: -11.64‰ V-PDB). Furthermore, every fifth sample was analysed in duplicate.

Mineralogy and $\delta^{13}C$ analyses of lithified carbonate nodules

The quantitative mineralogical compositions of weakly lithified nodules (in PC009) were determined by X-ray diffraction (XRD) on homogenized bulk-rock powders. Dried nodules were pulverized using agate planet milling for ~1 minute. Powders were analysed on a Bruker D8 Advance X-ray diffractometer using Cu-Kα radiation (40 kV/40 mA) at 3 to 75° 2θ range (0.02° 2θ steps; time/step = 1 second). Minerals were identified using the Diffrac.EVA 3.1 software and quantified using Rietveld modelling and the TOPAS 5.0 software (2 to 3 wt.% uncertainty). Subsamples of the XRD analysed powders were used for stable carbon analyses. The powders were reacted with anhydrous phosphoric acid in a GasBench II preparation line at University of Tartu, Estonia. The released CO_2 gas was analysed with a Delta V Advantage isotope ratio mass spectrometer (reproducibility for $\delta^{13}C$ was estimated ± 0.2‰).

Lipid biomarkers

Sediment samples for lipid biomarker analyses (only on PC021) were sampled with an alcohol-cleaned spatula and wrapped in aluminium foil and stored at -20°C. The total lipid extraction (TLE) was performed on ~20 g of sediment with ultrasonification in four solvents with decreasing polarity. The solvents used for extraction were methanol (MeOH) to dichloromethane (DCM) 2:1, MeOH to DCM 1:2 and two last steps using only DCM. The total lipid extract was saponified with NaOH. Fatty acids were methylated to fatty acid methyl esters (FAMEs) from the resulting solution after the neutral fraction was extracted. The neutral fraction was further separated into hydrocarbons, ketones, and alcohols. The alcohol fraction was derivatized to form trimethylsilyl (TMS) adducts

for analysis. Individual lipid compounds were analysed using a gas chromatograph (GC) (Thermo Scientific TRACE™ Ultra), equipped with a capillary column (Rxi-5ms, 50 m, 0.2mmID, 0.33 µm df), using helium as a carrier gas at a constant flow rate of 1 mL per min. The initial oven temperature was set to be 50°C, held for 2 min and then increased to 140°C at a rate of 10°C per min and held for 1 min. Finally, the temperature was increased to 300 °C at 4 °C per min. The final hold time was 160 min to analyse lipids with higher boiling points in the hydrocarbon and alcohol fractions. Concentrations were determined by flame-ionization detection (FID) against internal standards. Unknown compounds were identified with a quadrupole mass spectrometry (QMS) unit (Thermo Scientific DSQ II) linked to a gas chromatograph. Similarly, compound-specific stable carbon isotope ratios were determined using a magnetic sector isotope ratio mass spectrometry unit (Thermo Scientific Delta V Advantage) coupled to a gas chromatography setup with the same specifications as the above. The $\delta^{13}C$ values are reported against VPDB with an analytical error of ±1‰.

5.3 Pore water modelling

The transport-reaction model used in this work was developed following similar consideration as in Hong et al. (2014). We considered seven dissolved species including the isotopes of DIC (^{12}C-DIC and ^{13}C-DIC) and CH_4 (^{12}C-CH_4 and ^{13}C-CH_4) as well as sulphate, calcium, and ammonium. In addition, we included organic matter (POC) and authigenic calcium carbonate as well as their isotopic signatures in the model (^{12}C-POC, ^{13}C-POC, ^{12}C-carbonate, and ^{13}C-carbonate) to account for the observed changes in isotopic signatures. Diffusion of the solutes was accounted for using Fick's law with diffusion coefficients corrected for temperature and tortuosity (Boudreau, 1997). There are two types of aqueous fluid advection in the model. One is the burial of pore fluid as a result of sedimentation. The pore fluid burial velocity is calculated based on the reduction of porosity (Boudreau, 1997). Fluid advection also occurs due to changes in pressure with a velocity constrained by the shape of the measured pore fluid profiles. Burial of sediment particles was also included which was also calculated from porosity profiles (Pape et al., 2020). We considered six groups of reactions in this model:

1. Net anaerobic oxidation of methane (**AOM**) coupled to sulphate reduction (**SR**)
   $SO_4^{2-} + CH_4 \rightarrow HCO_3^- + HS^- + H_2O$.
2. Back flux reaction of AOM (Yoshinaga et al., 2014) (**AOM-CR**)
3. CO_2 reduction (methanogenesis) (**CR**)
4. Particulate organic carbon degradation through sulphate reduction (P**OC-SR**) and fermentation (**POC-ME**) (ME=methanogenesis)
   POC-SR: $TOC + 0.5SO_4 \rightarrow DIC + N/C\ NH_4$
   POC-ME: $TOC \rightarrow DIC + N/C\ NH_4$
5. Authigenic carbonate formation (carbonate precipitation **CP**)
   $DIC + Ca \leftrightarrow Carbonate$

6. Incorporation of DIC and CH_4 into biomass of anaerobic methanotrophic archaea, ANME, (DIC assimilation: **DIC-ASS**, CH_4 assimilation: **CH_4-ASS**)

There are isotopic fractionations associated with some of the reactions which were accounted for by slightly differentiating the kinetic constants of the ^{12}C- and ^{13}C-reactions (Rees, 1973). Detailed formulation of these reactions as well as the corresponding isotopic fractionation can be found in the supplementary information. We assumed seawater composition for the initial and top boundary conditions. We adopted either a no flux boundary condition (i.e., no exchange of material across the deepest cell in the model frame) or a fixed composition for the lower boundary condition. The choice of different types of lower boundary conditions depends on the conditions of the site and will be discussed later.

6 Results

6.1 Seafloor observations

The high-resolution bathymetric maps (Fig. 1C) reveal complex internal structures of the Lunde and Lomvi pockmarks with ca. 20 % of the area within both pockmarks containing bacterial mats and seep carbonates. Cores PC007 and PC009 are from the southwestern sector of Lomvi within a depression just next to a ridge structure. Both cores were retrieved from white sulfur oxidising bacterial mats (Fig. 2). PC017 and PC021 from Lunde were also retrieved from seafloor showing white bacterial mat traces but mostly black sediment patches (Fig. 2). The seafloor around the location of PC020 showed no signs of bacterial mats or other indications of gas-charged sediments.

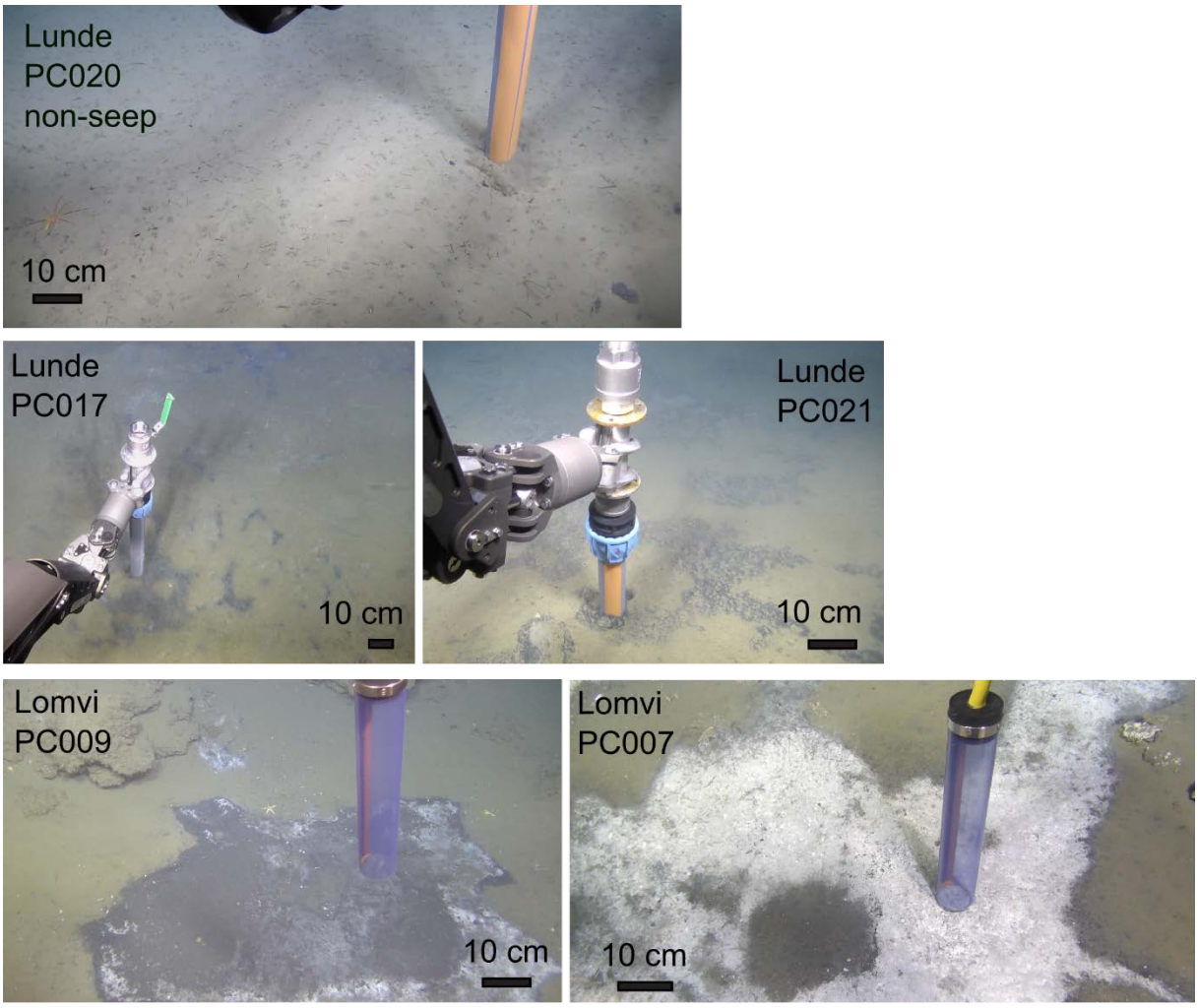

Figure 2:Seafloor images taken by the ROV during push core recovery. Note the white sulphur oxidizing bacterial mats and black sediment patches in all photos except for the non-seep site PC020.

6.2 Pore water geochemistry

Phosphate and ammonium concentrations were low throughout all investigated cores (below 11 µM PO_4^{3-} and below 30 µM NH_4^+) (Fig. 3, Table S3). The strongest rise in PO_4^{3-} concentration was observed in the non-seep core PC020 with an increase from 1 µM up to 9 µM within the upper 16 cm. Fe^{2+} and Mn^{2+} release to the pore water in the upper sediment could only be observed in cores PC021 and PC020 from the Lunde pockmark (Fig 3). Core PC021 shows a very narrow zone of dissolved Mn^{2+} in the upper 4 cm of the sediment. The non-seep core PC020 showed the most pronounced increases in dissolved Mn^{2+} and Fe^{2+}. Dissolved Fe^{2+} was above 1µM in the upper 26 cm of the core with a peak of 21 µM at 10 cmbsf. Dissolved Mn^{2+} is present in the pore water throughout core PC020 but shows a peak of 14 µM at 8cmbsf. In PC017 dissolved Mn^{2+} is present in the pore water below 15 cm.

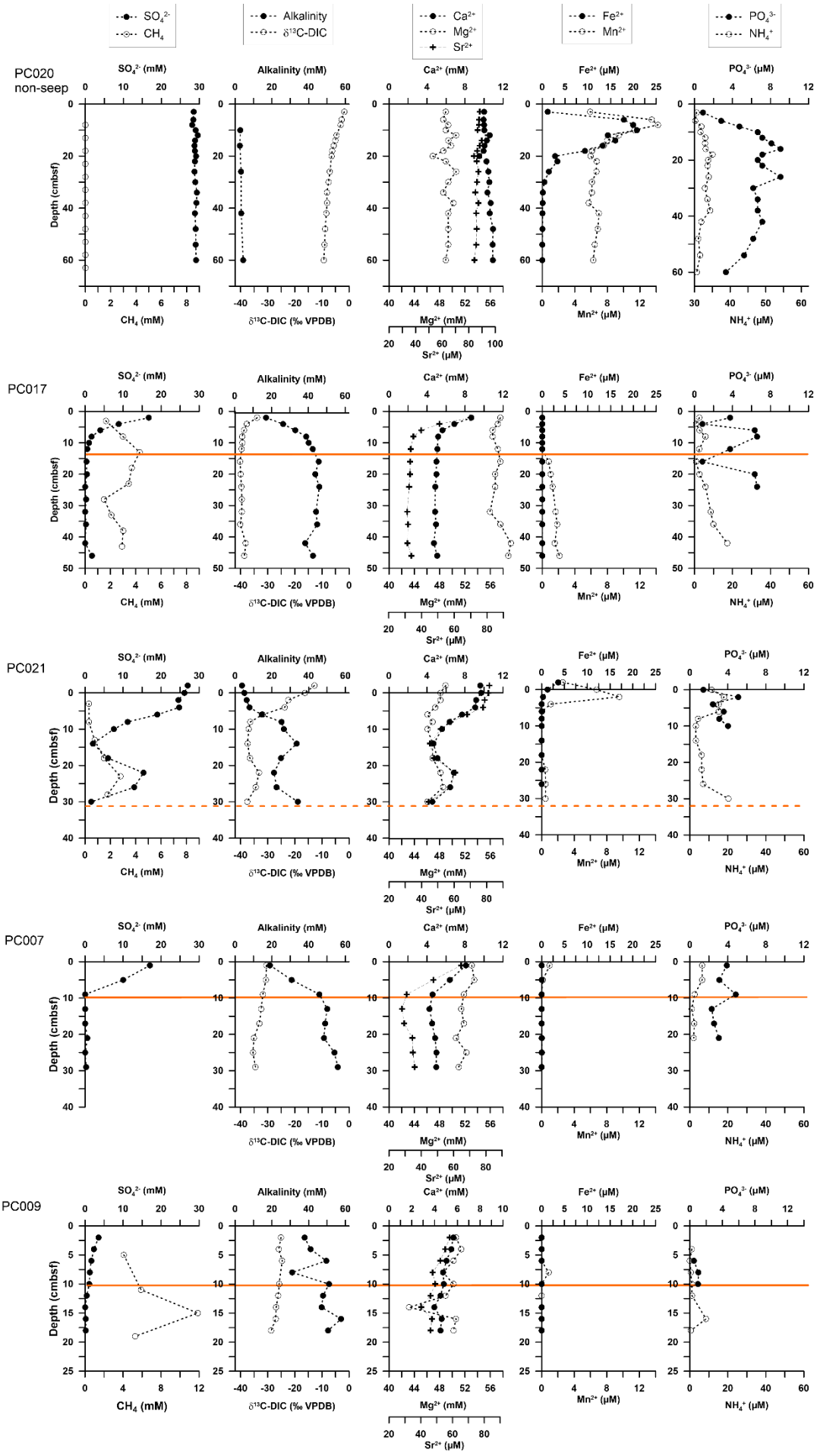
PC020
non-seep
PC017
PC021
PC007
PC009
SO4 2- (mM)
CH4 (mM)
Alkalinity (mM)
δ13C-DIC (‰ VPDB)
Ca2+ (mM)
Mg2+ (mM)
Sr2+ (μM)
Fe2+ (μM)
Mn2+ (μM)
PO4 3- (μM)
NH4+ (μM)
Depth (cmbsf)

Figure 3:Pore water concentration profiles of PC007, PC009, PC017, PC020 and PC021. Sulphate and δ^{13}C-DIC profiles adopted from (Dessandier et al., 2020). The orange line represents the depth at which sulphate drops below detection limit. In PC020 sulphate concentration is high throughout the core. In PC021 we assume sulphate is depleted just below our deepest sample, thus the orange line is dashed.

Strong decreases in SO_4^{2-} concentrations were observed in four out of the five studied push cores: PC007 and PC009 from Lomvi pockmark, and PC017 and PC021 from Lunde pockmark. Our non-seep core PC020 showed no decrease in SO_4^{2-} concentration down to a depth of at least 60 cmbsf indicating little sulphate reduction at this site (Fig. 3). Complex sulphate profiles in some of our cores hinder determining the exact depth of the sulphate-methane-transition-zone (SMT (e.g. Boetius et al., 2000; Iversen and Jørgensen, 1985)). Thus, we indicate the depth of sulphate depletion in Fig. 3. PC007 showed a linear decrease in sulphate concentration from 17 mM to below detection limit within the upper 9 cmbsf. Sulphate concentration was 3.6 mM at 2 cmbsf in core PC009, followed by a slow decrease until reaching the detection limit at 14 cmbsf. In PC017 SO_4^{2-} concentration decreased from 17 mM at 2 cmbsf to below 1 mM at 12 cmbsf (Fig. 3). In PC021, SO_4^{2-} concentrations decreased from 27 mM in the bottom water to 2 mM at 14 cmbsf with another SO_4^{2-} peak at 22 cmbsf. Headspace methane measurements confirm the presence of methane in the shallow sediments with up to 11.9 mM CH_4 in PC009, up to 4 mM in PC017, up to 3 mM in PC021 and below 0.009 mM throughout non-seep core PC020. PC009 showed highest TA values up to 57.7 mM at 16 cm, followed by PC007 (TA up to 50.1 mM) and PC017 (TA up to 46 mM). At non-seep site PC020 TA increased to only 4.4. mM at 60 cm, indicating very limited production of TA (Fig. 3); seawater TA is approximately 2 mM. In PC017 δ^{13}C-DIC values became progressively lower downcore and reached values as low as -40‰. Below 10 cm depth there was very little variation in the δ^{13}C-DIC profile of PC017. Also, the profiles of PC007, PC009 showed little variation with depth and overall low values: PC007 (-35.4‰) and PC009 (-28.7‰). PC021 showed a decreasing trend of δ^{13}C-DIC in the upper 10 cm and values down to -37.6‰ below that. In non-seep core PC020 the δ^{13}C -DIC only decreased down to -10‰ (Fig. 3). In our non-seep core PC020 dissolved Ca^{2+}, Mg^{2+} and Sr^{2+} remained close to seawater concentration throughout the core (average Ca^{2+}: 10mM, average Mg^{2+}: 49.2 mM, average Sr^{2+}: 87.1 µM). In contrast, in cores PC007, PC009, PC017 and PC021 Ca^{2+} concentrations decreased to between 4 and 5 mM, i.e. about half the seawater concentration. Sr^{2+} concentrations decreased to between 28 and 44 µM, i.e. to half or even a third of seawater concentration (Fig. 3). Mg^{2+} concentrations did not show a coherent pattern.

6.3 Gas isotopes

We measured methane headspace concentration and methane carbon isotopes (δ^{13}C-CH_4 in ‰ VPDB) on altogether 29 samples from four different push cores, PC009, PC017, PC021 and PC020 (Fig. 4, Table S4). The results showed large variability in δ^{13}C-CH_4 from -77.4‰ (PC017) to -51.4‰ (PC020). δ^{13}C-CH_4 values in

PC009 varied between -69‰ and -65.8‰, and in PC021 the two lowest samples were below -72‰, whereas all samples above 18 cmbsf where above -64‰ (Fig. 4A). We obtained methane hydrogen isotopic composition (δ^2H-CH_4 in ‰ VSMOW) on three push cores (PC009, PC017 and PC021). The methane concentrations in PC020 were too low for hydrogen isotope determination. The δ^2H-CH_4 values were very similar in all three cores and varied between -189‰ and -163‰ SMOW (Fig. 4B).

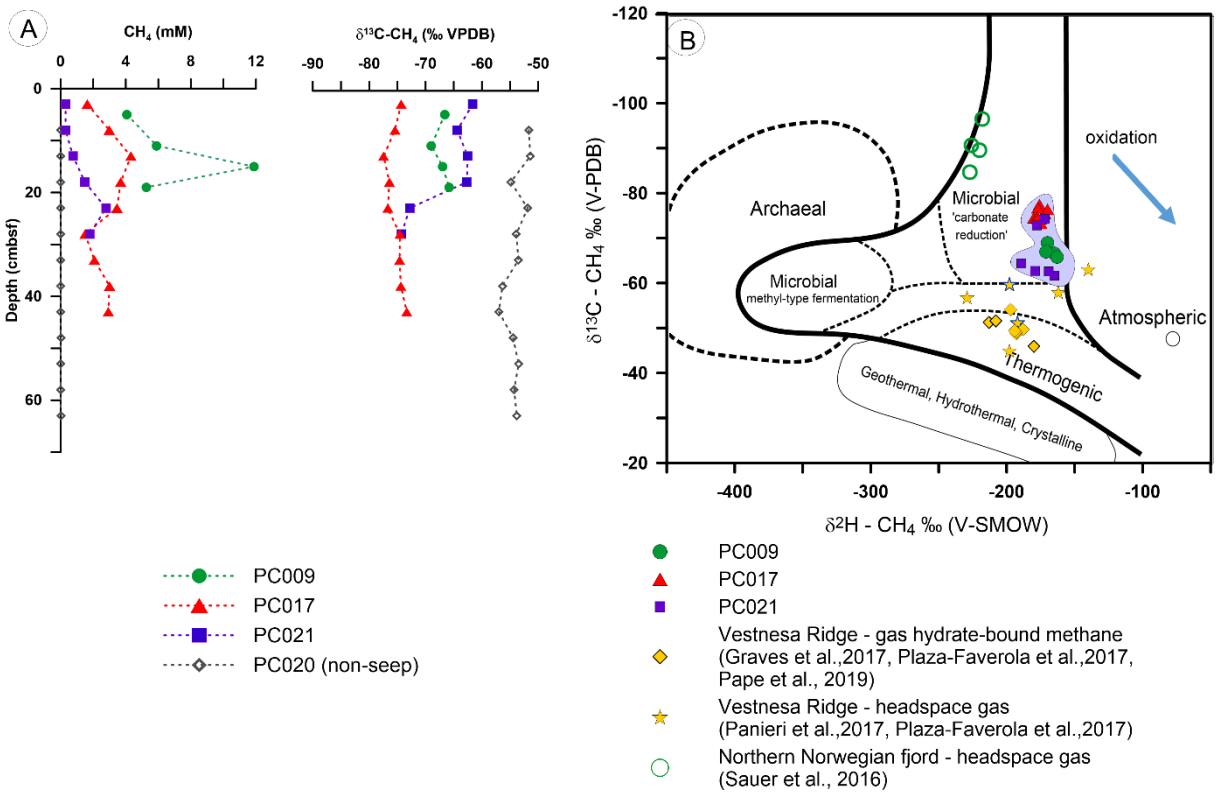

Figure 4: A)Methane concentration and δ^{13}C-CH_4 profiles from the push cores of Lunde (PC017, PC020, PC021) and Lomvi (PC009) pockmark and B) plot of δ^{13}C-CH_4 versus δ^2H-CH_4 indicating the different methane sources (after Whiticar, 1999). Gas data for comparison is from the following publications: (Graves et al., 2017; Panieri et al., 2017; Pape et al., 2020; Plaza-Faverola et al., 2017; Sauer et al., 2016). The blue arrow indicates the direction of isotopic fractionation during oxidation.

We also determined ethane carbon isotopes (δ^{13}C-C_2H_6) on three push cores (Fig. 5). The values are similar in all three push cores ranging between -28.7‰ and -25.2‰.

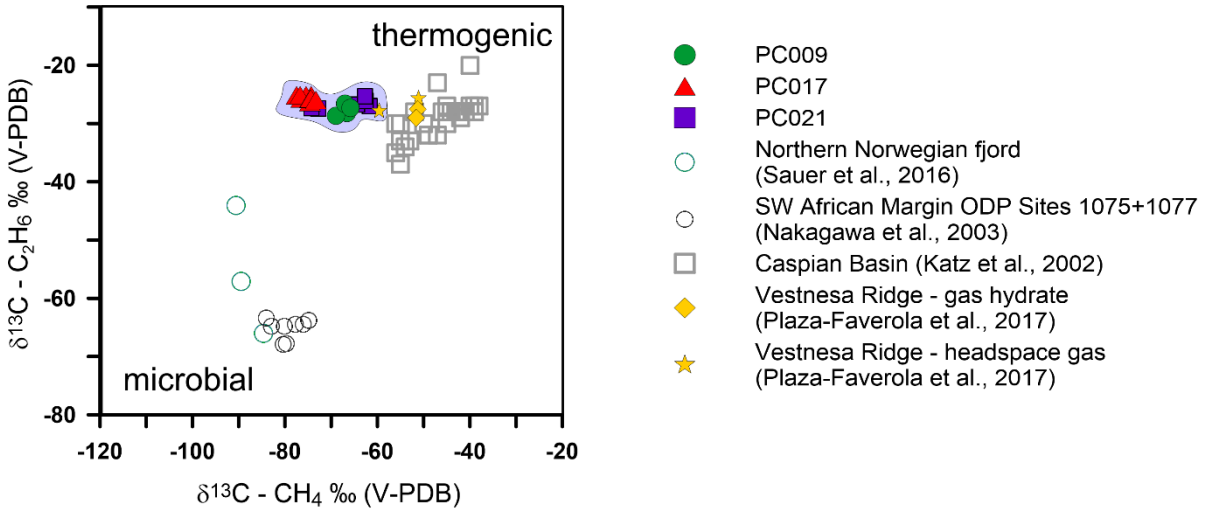

355

356 *Figure 5: An ethane vs. methane $\delta^{13}C$ plot including data from PC009, PC017 and PC021. For comparison we plotted data*
357 *from Vestnesa Ridge (Plaza-Faverola et al.,2017), from a northern Norwegian fjord and ODP sites offshore SW Africa with*
358 *a microbial signature (Nakagawa et al., 2003; Sauer et al., 2016), and from known thermogenic gas in the Caspian Basin*
359 *(Katz et al., 2002).*

360 **6.4 Sediment characteristics**

361 6.4.1 Organic carbon, inorganic carbon, and total nitrogen content

362 We determined total carbon, total organic carbon and total nitrogen on 92 sediment samples from five push cores
363 (Table S5). The average TOC content was 1.8 wt% in PC007 and PC017, 1.5 wt% on average in PC009 and
364 PC021, and 1.3 wt% in non-seep core PC020 (Fig. 6). TN content varied between 0.13 wt% and 0.29 wt%
365 (average 0.21 wt%). The atomic Corg/Ntot ratios varied between 6.7 and 11 with an average of 8.7 and showed
366 no specific downcore trends in any of the push cores (Fig. 6).

367

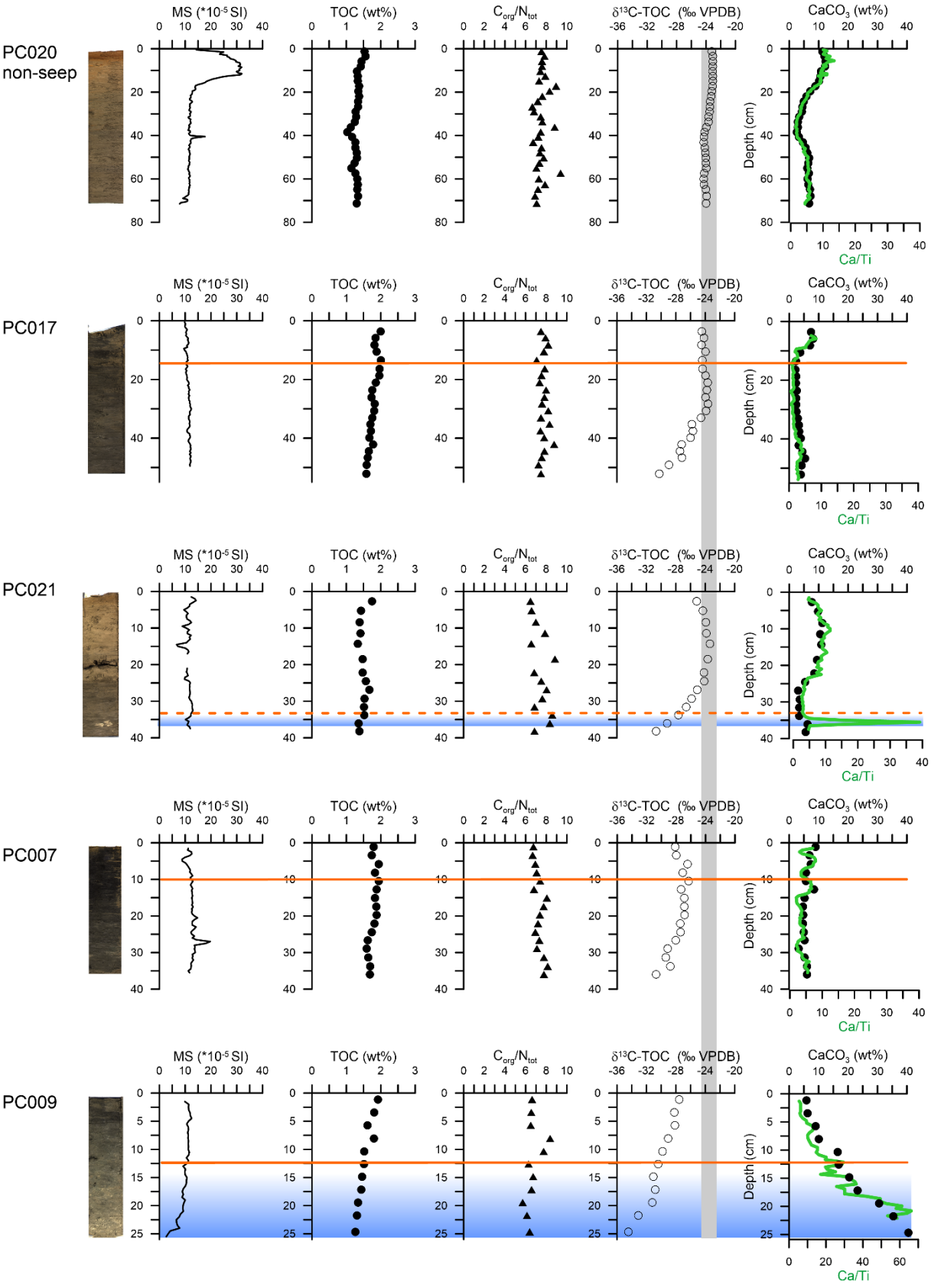

Figure 6: Sediment characteristics and geochemical profiles of push cores from Lunde pockmark (PC020, PC017, PC021) and Lomvi pockmark (PC007, PC009). From left to right: high resolution core photos, magnetic susceptibility (MS),total organic carbon content (TOC), organic carbon/total nitrogen ratio (C_{org}/N_{tot}), stable carbon isotope ratio of total organic carbon ($\delta^{13}C$ -TOC), $CaCO_3$ content and the Ca/Ti ratio from XRF scans (green line). The orange lines denote the depth of

sulphate depletion inferred from the pore water profiles. The blue fields indicate intervals with high carbonate content inferred from the Ca/Ti profiles and the occurrence of seep carbonate nodules. The grey vertical bar in the δ^{13}C-TOC plots marks the "background" value inferred from non-seep core PC020.

Total inorganic carbon average values varied between 0.5 wt% (PC017) and 2.3 wt% (PC009). $CaCO_3$ content calculated from the inorganic carbon content varied between 3.8 wt% (PC017) and 19.5 wt% (PC009) (Table 2). δ^{13}C-TOC values showed larger differences between cores and specific downcore trends (Fig. 6). The non-seep core PC020 showed the least variation in δ^{13}C-TOC values, with a range from -24.3‰ to -23.1‰ (average: -23.7‰). All other cores showed strong decreases in δ^{13}C-TOC downcore with values lower than -30‰, with lowest values at the base of the cores (PC007: -30.7‰, PC009: -34.5‰, PC017: -30.2‰, PC021: -30.7‰).

Table 2: Average values of total organic carbon (TOC), δ^{13}C-TOC, total nitrogen (TN), total inorganic carbon (TIC), and calcium carbonate content calculated from inorganic carbon ($CaCO_3$).

			TOC (wt%)	δ^{13}C-TOC	TN (wt%)	TIC (wt%)	$CaCO_3$ (wt%)
Lunde	PC020	non-seep	1.3	-23.7	0.17	0.8	6.9
Lunde	PC017	seep	1.8	-25.3	0.23	0.5	3.8
Lunde	PC021	seep	1.5	-25.5	0.20	0.8	7.0
Lomvi	PC007	seep	1.8	-27.8	0.24	0.7	5.8
Lomvi	PC009	seep	1.5	-30.3	0.23	2.3	19.5

6.4.2 Sediment core images, carbonate content and magnetic susceptibility

The core images of the five push cores (Fig. 6) show a range in colours and lightness. PC009 and PC021 are much lighter than PC007 and PC017. This difference corresponds well with their different $CaCO_3$ content (Fig. 6). PC020 shows some distinct reddish-brown to yellowish-brown coloration of the sediments in the top centimetres probably indicating the presence of iron oxides (Schwertmann and Fitzpatrick, 1992). The inferred presence of iron oxides corresponds well with the peak in magnetic susceptibility in the upper 15 cm of PC020, a general measure for the concentration of magnetic minerals in marine sediments (Dekkers, 1978). All other cores show very little variation in magnetic susceptibility and overall low values (below $15x10^{-5}$ SI).

6.4.3 Diagenetic carbonate nodules

Figure 6 shows the $CaCO_3$ wt% (calculated from total inorganic carbon) and the Ca/Ti ratio (from XRF scans, green line) for all cores. The two analyses correspond very well in each core, showing the same downcore trends. Only in PC021 there is a peak in Ca/Ti at around 35 cmbsf which is not resolved in the discrete $CaCO_3$. We found indications for carbonate nodules in core PC021 at around 35 cmbsf (peak in Ca/Ti, white coloration of the core) and in core PC009 below 10 cmbsf (increasing abundance with depth). In PC009 the proportion of calculated $CaCO_3$ content reaches up to around 40 wt% at the base of the core. Only in this core we found

carbonate nodules large and abundant enough to be extracted by sieving for XRD and carbon isotope analyses (Table 3, Fig. 7). The δ^{13}C-carbonate values range between -26.6‰ and -29.4‰ and correspond well with the present-day pore water δ^{13}C-DIC values at the base of the core (Fig. 7). The carbonate mineralogy is mainly Mg-calcite and aragonite, with only minor proportions of calcite (Table 3, Fig. 7). The main lithogenic components were quartz, plagioclase, illite and muscovite (Table 3).

Table 3: Results of quantitative XRD analyses and δ^{13}C-carbonate analyses of the authigenic seep carbonates from PC009.

				XRD						
	Interval top (cmbsf)	Interval bottom (cmbsf)	δ^{13}C (‰ V-PDB)	Mg-Calcite	Aragonite	Calcite	Quartz	Plagioclase	Illite/ Muscovite	Chlorite
PC009	13.70	16.00	-27.75	72			12	4	9	3
PC009	16.00	18.30	-28.61	77			11	4	6	2
PC009	18.30	20.60	-26.57	38		4	31	7	14	5
PC009	20.60	22.90	-28.51	40	24	4	12	5	9	5
PC009	22.90	26.40	-29.42	35	31	4	13	5	7	5

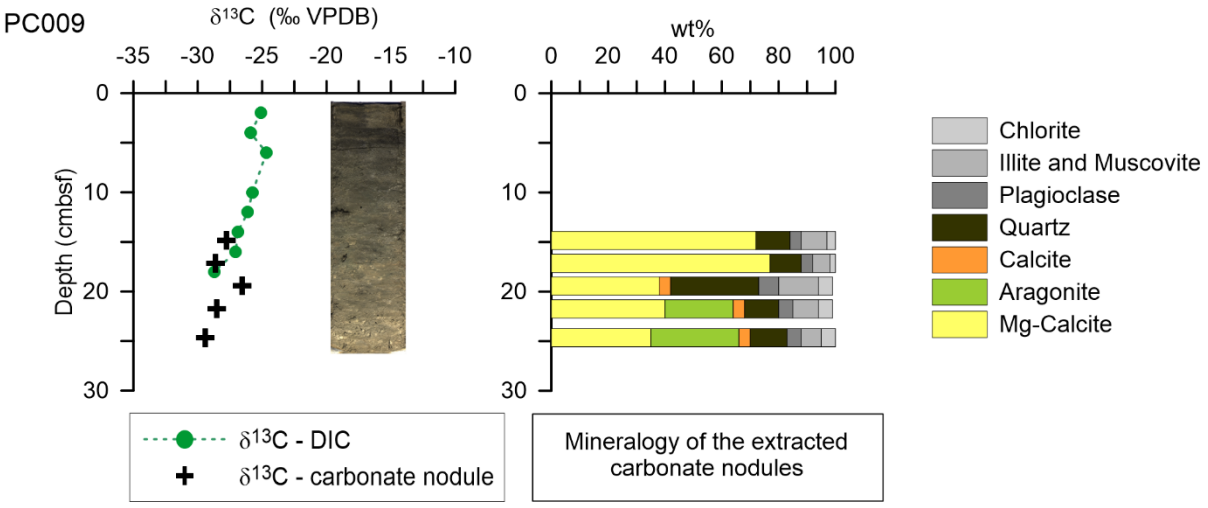

Figure 7:left:δ^{13}C values of pore water DIC (green dots) and of carbonate nodules (black crosses) of PC009 including a colour photo of the core, right: mineralogy from quantitative XRD analysis of the carbonate nodules extracted from PC009.

The occurrence of the carbonate nodules in PC009 corresponds very well with the low δ^{13}C -TOC values in this core. Also, in Core PC021 a peak in the Ca/Ti record corresponds to the depth of low δ^{13}C -TOC values (Fig. 6).

6.4.4 Lipid biomarkers in PC021

PC021 was sampled for the quantification and compound-specific δ^{13}C analysis of archaeal lipid biomarkers, namely archaeol and sn2-hydroxyarchaeol, which are isoprenoid glycerol diethers. Their compound-specific δ^{13}C values have been widely used as a tool to identify the presence of AOM communities (e.g. Niemann and Elvert, 2008, and references therein). The archaeol content showed peaks at around 8 cm and 36-38 cm sediment depth with 0.33 µg/g and 0.63 µg/g, respectively. These peaks are less pronounced but also visible in the sn2-hydroxyarchaeol content (Table 4). The δ^{13}C -of archaeol and sn2-hydroxyarchaeol show low values (down to -

97‰ and -110‰, respectively) in the areas with elevated lipid biomarker content, confirming their link with the presence of ANME communities.

Table 4: Content of the lipid biomarkers archaeol and sn2-hydroxyarchaeol and their compound-specific $\delta^{13}C$ values measured on samples from PC021.

Sediment depth (cm)	archaeol (µg/g)	sn2-hydroxyarchaeol (µg/g)	$\delta^{13}C$-archaeol (‰ VPDB)	$\delta^{13}C$-sn2-hydroxyarchaeol (‰ VPDB)
2.7	0.09	0.04		
5.3	0.07	0.09	-67.4	-100.4
8.5	0.33	0.13	-78.7	
11.5	0.05	0.06	-90.5	-90.8
14.3	0.06	0.07	-60.0	-59.3
18.5	0.08	0.03	-63.6	
21.0	0.18	0.20	-82.0	-78.3
24.6	0.12	0.06	-68.9	
26.9	0.28	0.14	-66.8	-82.7
29.3	0.16	0.01	-82.9	
31.6	0.13	0.00	-87.6	-71.5
33.8	0.20	0.00	-71.6	-67.7
36.1	0.63	0.22	-90.6	-110.1
38.2	0.41	0.09	-97.3	-99.5

7 Discussion

7.1 Early diagenetic sequence in shallow sediments and fluid flow indications

Pore water sulphate concentrations are controlled by two main processes, 1) the degradation of organic matter via SO_4^{2-} reduction (POC-SR) and 2) sulphate-dependent anaerobic oxidation of methane (AOM)(e.g. Reeburgh, 2003). All cores from the Lunde and Lomvi pockmark showed low concentrations of ammonium and phosphate, which suggests low organic matter degradation rates (Froelich et al., 1979). Similar concentrations were reported from cold seeps south of Svalbard and the northern Norwegian margin (Hong et al., 2020). Peaks in Fe^{2+} and Mn^{2+} (as in PC020 and PC021) are commonly also associated with organic matter degradation utilizing Mn and Fe (oxyhydr)oxides as electron acceptors and releasing dissolved Mn^{2+} and Fe^{2+} to the pore water (Froelich et al., 1979). Supported by the low ammonium and phosphate concentrations we conclude that the sulphate profiles are controlled mainly by ascending methane through sulphate-dependent-AOM. Anaerobic oxidation of methane leads to the production of bicarbonate documented by the strong increase in the alkalinity in our seep cores. Carbonate alkalinity can induce the formation of authigenic seep carbonates, as observed in PC009, including calcite, aragonite, high- and low-magnesium calcite (Aloisi et al., 2002; Bayon et al., 2009; Bian et al., 2013; Gieskes et al., 2005; Sauer et al., 2017; Teichert et al., 2003).

Another indicator of AOM observed in all seep cores is the decrease in δ^{13}C-DIC to low values which cannot be explained solely by the degradation of organic matter (except in non-seep PC020). It requires the transformation of isotopically light methane to dissolved inorganic carbon to explain δ^{13}C-DIC values as low as -40‰ (PC017). Below the SMT, an increase in δ^{13}C-DIC has often been observed in other seep settings (e.g. Haese et al., 2003; Hong et al., 2014; Pape et al., 2020; Paull et al., 2000; Sauer et al., 2015), which is commonly attributed to methanogenesis by CO_2 reduction, preferentially consuming ^{13}C-depleted CO_2. This trend is however not observed in our cores (Fig. 3, second column). Instead the δ^{13}C-DIC approaches or maintains low values even well below the SMT.

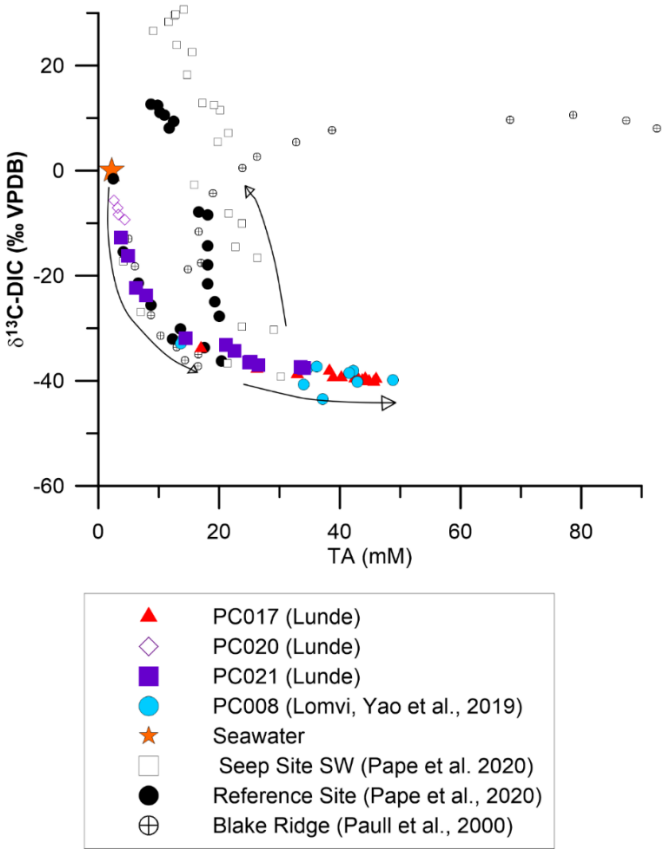

Figure 8: Scatter plot comparing pore water δ^{13}C-DIC to total alkalinity (TA) values in different cores. Vestnesa Ridge data: Pape et al. (2020)(MeBo seep site SW c. 15 m and reference site c. 62 m), and Yao et al. (2019) (PC008, push core c. 35 cm), Blake Ridge ODP Site 994: Paull et al. (2000) (ODP Hole 994, c. 700 m). The orange star marks seawater values. The arrows indicate different downcore trends. The total alkalinity values around the SMT at Seep Site SW, Reference Site, and Blake Ridge range between 15-30 mM.

To emphasize this unusual downcore δ^{13}C-DIC trend in our pore water profiles, we compare the patterns of δ^{13}C-DIC plotted against TA with published data from the Vestnesa MeBo Seep Site SW and reference site (Pape et al., 2020) and Blake Ridge (Paull et al., 2000). In Fig. 8 most of the cores show a trend departing from near-seawater values (orange star) and subsequently show the expected downcore addition of ^{13}C-depleted DIC from AOM (PC021, Blake Ridge, Vestnesa Seep- and Reference Site) or by organic matter degradation (PC020).

This results in an increase in alkalinity and at the same time lowering of δ^{13}C-DIC values (arrow starting at the orange star). Below the SMT in the cores from Vestnesa reference and Seep Site SW, and Blake Ridge, a progressive removal of ^{13}C-depleted DIC can be observed, indicated by the arrow pointing towards high δ^{13}C-DIC values (Fig. 8), explained by CO_2 reduction. In contrast, the push cores from our study and PC008 from Yao et al. (2019) show a different downcore trend, indicated by the arrow pointing to high TA values. Below the SMT, total alkalinity still increases and δ^{13}C-DIC values are continuing to decrease slightly or remain close to values found at the SMT (Fig. 3 and 8). Assuming TA is only produced from AOM the maximum concentration is expected around the SMT, but some of our cores show higher TA below the current SMT (PC007, Fig. 3). In order to investigate the processes creating the observed δ^{13}C profiles in our cores, we applied a transport-reaction model on both the MeBo Seep site SW (Pape et al., 2020) and our core PC017. We first applied the model to the MeBo Seep site SW with a common set of reactions, such as AOM, carbonate precipitation and CO_2 reduction, which have been shown to occur based on the box modelling performed by Pape et al. (2020). Our model was able to reproduce the measured pore water profiles observed at MeBo Seep Site SW (Fig. 9) with the increase in DIC concentration in the uppermost meter that can be attributed to sulphate dependent AOM which also stimulates carbonate precipitation as reflected by the drawdown in calcium concentration (see also the rates of AOM and carbonate precipitation in Fig. 9). The downcore decrease in δ^{13}C-DIC in the upper meter results from ^{13}C-depleted DIC production during AOM while the associated decrease in δ^{13}C-CH_4 within the same interval reflects the back-reaction of AOM in the model which produces ^{13}C-depleted CH_4 (Yoshinaga et al., 2014). Below the SMT the progressive increase in δ^{13}C-DIC can be modelled by assigning an in-situ methanogenesis (POC-ME in Fig. 9) and a fixed fluid composition for the lower boundary condition at 5 mbsf ([DIC]=18 mM and δ^{13}C-DIC=0‰). Such a lower boundary composition reflects both the addition of DIC through organic carbon fermentation and methanogenesis via CO_2 reduction. In terms of δ^{13}C-CH_4 below the SMT, little downcore variation is predicted by the model except for the depths around the SMT. Such results indicate that the isotopic signatures of methane largely reflect the source composition of methane from depth at this site, also observed by Pape et al. (2020). We show that the data can be satisfactorily fitted with no additional fluid flow included, only advection due to sediment burial (Fig. 9). This agrees with the findings from Pape et al. (2020) that these pore water profiles can be accounted for with a box model which assumes no advection.

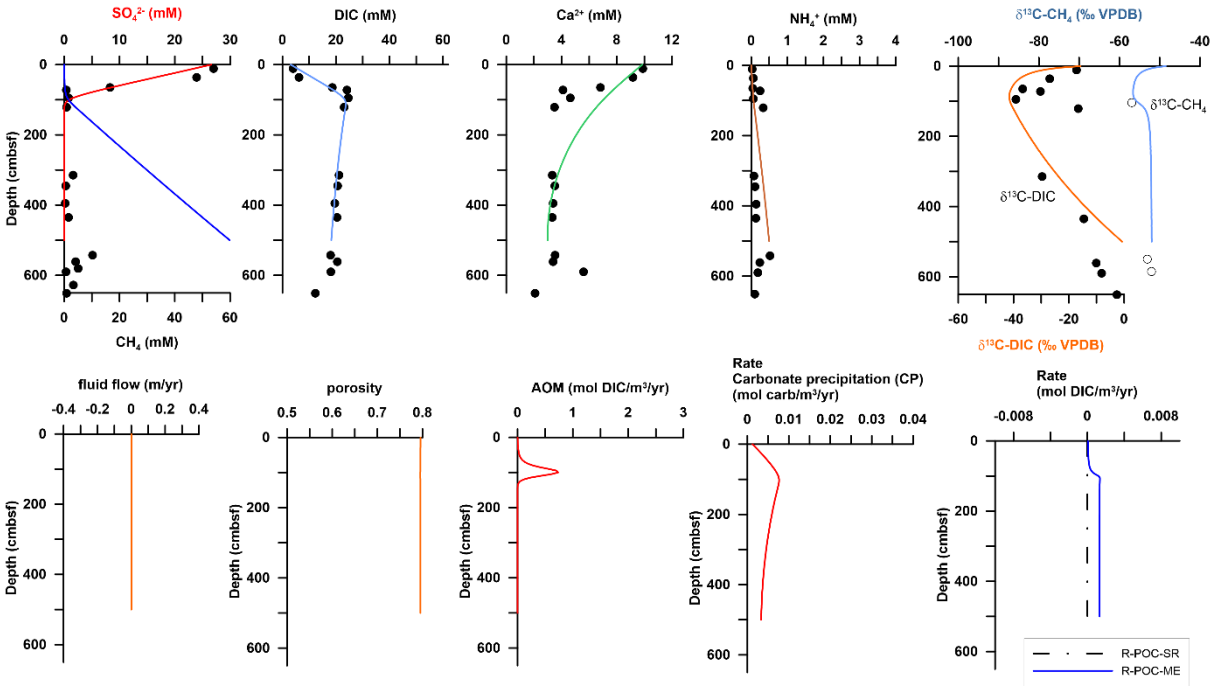

Figure 9: Modelling results for MeBo Seep Site SW (Pape et al., 2020) (pore water advection is only due to sediment burial and compaction, no additional fluid flow). The total fluid flow in the lower left graph is $3.02x10^{-4}$ m/yr. The black dots represent measured pore water composition (Pape et al., 2020), the solid lines represent the best fit from our model. The upper right graph includes measured data for δ^{13}C-DIC (filled dots) and δ^{13}C-CH_4 (circles). The lower right graph includes the depth profiles of the rates of organoclastic sulphate reduction (R-POC-SR) and organic matter degradation by fermentation (R-POC-ME). Rates of AOM, POC-SR and POC-ME are all expressed in mol DIC/m^3/yr to make them easier to compare.

We then applied our model to PC017, the longest push core besides the non-seep core, showing the least complex pore water profiles. In core PC017 the depth of sulphate depletion is around 13 cmbsf whereas it is at ~110 cm at MeBo Seep site SW. We find that the only way to fit the measured pore water profiles was to 1) reduce the number of reactions included in the model, 2) assign a high fluid advection rate and 3) assign a fixed composition for the lower boundary condition. We tested two other model setups with no external fluid advection (Fig. S1), and with neither CO_2 reduction nor external fluid advection (Fig S2), but found unsatisfactory fits for DIC, Ca^{2+} and δ^{13}C-DIC profiles in both tests (supplementary information).

In Fig. 10 we show that the pore water profiles, especially the DIC concentration and δ^{13}C-DIC pattern can only be explained when including fast fluid advection (0.2 m/yr) of a fluid containing no sulphate, abundant DIC and methane (40 mM and 6 mM, respectively, both with relatively low δ^{13}C values), low concentrations of ammonium (20 µM) as well as calcium (5 mM). This composition of the ascending fluid is used as the lower boundary condition. A fraction of the DIC is consumed by CO_2 reduction (see R-CR in Fig. 10), but it does not significantly influence the overall downcore δ^{13}C-DIC signature, i.e. there is only little increase in δ^{13}C-DIC with depth. The minimal increase in δ^{13}C-DIC with depth in PC017 can be explained by the influence of the ascending fluid which dominates the δ^{13}C-DIC signature. The amount of methane produced by CO_2 reduction

(with low δ^{13}C-CH_4 values) is however enough to cause a local minimum in δ^{13}C-CH_4 values in the PC017 profile at around 15 cm where the highest rate of CO_2 reduction is estimated (Fig. 10). This result means that the addition of methane through CO_2 reduction is significant enough, compared to the concentration of methane transported in the ascending fluid, to influence the overall δ^{13}C-CH_4 signature.

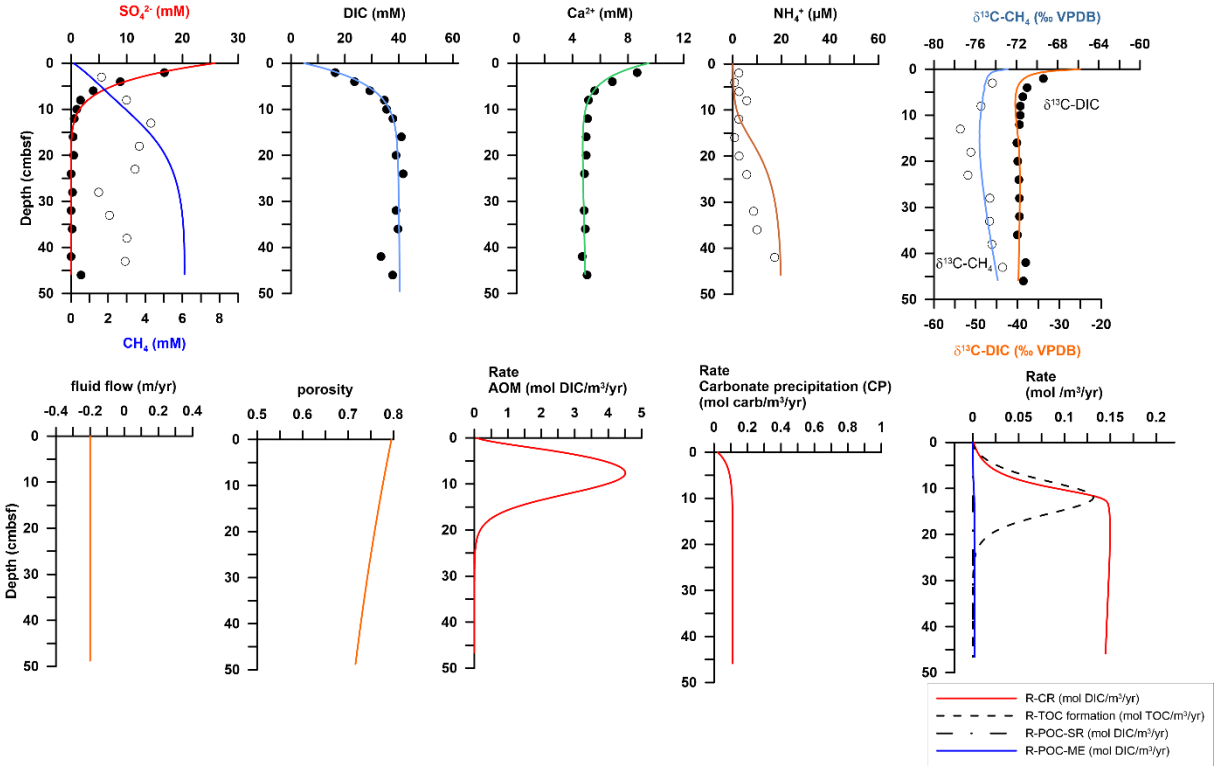

Figure 10: Modelling results for PC017 with a total fluid advection rate of 0.2 m/yr. The black dots and circles represent measured pore water data, the solid lines represent the best fit of our model. The lower right graph includes the depth profiles of the rates of CO_2 reduction (R-CR) organoclastic sulphate reduction (R-POC-SR) and organic matter degradation by fermentation (R-POC-ME), and organic matter formation by the AOM microbial consortium (R-POC formation). Rates of AOM, POC-SR, POC-ME and R-CR are all expressed in mol DIC/m^3/yr to make them easier to compare.

The phase of the fluid and mode of transport are critical in terms of the effectiveness of the biological benthic methane filter, i.e. how the microbial community can utilize the methane. Dissolved methane can be transported via diffusion and/or by advection of the pore water itself. Even though diffusion of methane is ubiquitous and occurs wherever there is a concentration gradient, there is usually very limited amounts of methane reaching the sediment-water interface in diffusion-dominated environments due to the efficient AOM (e.g. Egger et al., 2018). Advection of aqueous fluid with high dissolved methane concentration, however, can transport considerable amounts of methane towards the sediment-water interface (e.g. Luff et al., 2004; Stranne et al., 2019). Gas advection can also cause large amounts of methane to escape from the sediment through fractures or channels (MacDonald et al., 2002). Previous studies have shown that Lunde and Lomvi pockmark are characterized by diffusion, focussed fluid flow and methane transported in the gas phase (Hong et al., 2016; Panieri et al., 2017;

Pape et al., 2020; Yao et al., 2019). With our model we show that at site PC017 it requires a fast-moving aqueous fluid with dissolved methane to explain the observed pore water profiles. Given the constant δ^{13}C-DIC profiles we suggest that cores PC007, PC009, and PC008 (Yao et al., 2019) were dominated by aqueous fluid advection as well. High methane concentration and low δ^{13}C-DIC downcore variation in PC009 indicates especially efficient aqueous fluid advection. Worth noticing, our model predicts that only 6 mM of dissolved methane in the ascending pore water is enough to induce the observed change in fluid composition, a methane concentration that is far lower than what is required to form gas hydrate given the 1200m water depth. Pape et al. (2020) documented the presence of gas hydrate as shallow as 45 cmbsf from Vestnesa Ridge, and also at Storfjordrenna south of Svalbard, gas hydrate was observed at 35 cmbsf (Klasek et al., 2020). The shallow SMT at our investigated sites, but the absence of gas hydrate in all of our cores seems to support the relatively lower concentration of dissolved methane derived by our model.

In addition, we conducted a sensitivity test by varying the total fluid advection rate to investigate how the fluxes of the different solutes in the pore water, especially methane, vary (Table 5). This is done based on the model results from PC017. At a total advection rate of 0.2 m/yr, which is needed to reproduce our pore water profiles, 67% of methane entering our sediment core at the bottom of the core will pass the sediment water interface and escape into the water column. This is in stark contrast to MeBo Seep Site SW where only 1% of methane entering at the bottom of the core will leave the sediment into the water column. Our results are in agreement with previous modelling studies of methane transport across the sediment water interface (Stranne et al., 2019; Wallmann et al., 2006) and again emphasize the critical role of aqueous fluid advection..

Table 5: Model results of methane flux at the sediment water interface and at the bottom of the core (PC017) depending on the advection rate. The last line shows the results from MeBo Seep Site SW.

total advection rate	flux at the seafloor	flux at the bottom of the core	
m/yr	$CH_4/m_2/yr$	$CH_4/m_2/yr$	**% of CH_4 leaving sediments**
0.2	0.57	0.85	**67%**
0.15	0.34	0.64	**53%**
0.1	0.17	0.45	**37%**
0.05	0.06	0.33	**18%**
0.01	0.02	0.38	**6%**
0.001	0.02	0.41	**4%**
0.0001	0.02	0.42	**4%**
MeBo Seep Site SW	0.00	0.23	**1%**

549

550 At certain sites within the pockmarks Lunde and Lomvi methane is bypassing AOM/the benthic methane filter,
551 otherwise there would be no acoustic gas flares detected in the water column (e.g. Panieri et al., 2017). Methane
552 gas is not available for microbial utilization, therefor the microbial filter is always damned to fail when gas
553 migrates (e.g. Luff and Wallmann, 2003; Treude et al., 2003). Furthermore, Yao et al. (2019) showed that gas
554 advection along mini-fractures can rapidly increase methane concentrations in shallow sediments and play an
555 important role in modulating methane dynamics in shallow sediments. However, our push cores allow for the
556 first time to show and quantify considerable dissolved methane escape from the sediment at Vestnesa Ridge
557 based on pore water profiles. Two studies that have investigated pore water profiles from Vestnesa Ridge by
558 modelling (Hong et al., 2016; Pape et al., 2020) both suggest that at the investigated sites the AOM benthic
559 methane filter is effectively preventing dissolved methane from entering the water column. In contrast, our push
560 cores show that a significant amount of dissolved methane is passing the sediment-water interface (Table 5).
561 This also highlights the value of core sampling with video guidance, in this case the use of an ROV, which
562 allows to specifically target sites with methane seepage indicators (e.g. bacterial mats).

563 **7.2 Organic matter origin and past changes in methane flux**

564 Both the content and $\delta^{13}C$ signature of TOC in our push cores are more extreme compared to previously
565 published data from Vestnesa Ridge. Pape et al. (2020) report TOC values ranging from 0.51 to 1.27 wt% at
566 MeBo Seep site SW (Lunde pockmark) whereas in our push cores from seep locations we measured TOC as
567 high as 2 wt% (Fig. 6). Furthermore, $\delta^{13}C$-TOC values are as low as -34.5‰ in PC009, such low values have not
568 been reported from Vestnesa Ridge previously. Similar $\delta^{13}C$ values of organic matter extracted from a seep site
569 (-33‰) have been reported from the Eel River Basin offshore northern California (Hinrichs et al., 1999).
570 Common tools to determine the origin of organic matter in sediments are the Corg/Ntot ratio and $\delta^{13}C$-TOC
571 values. However, this approach is limited to regions where simple mixing between marine and terrestrial organic
572 matter is the case. At Vestnesa Ridge the use of Corg/Ntot ratios and $\delta^{13}C$-TOC values to determine organic
573 matter sources is complicated by the contribution of seep-endemic methanotrophic organisms. We interpret the
574 negative trends in $\delta^{13}C$-TOC in our push cores as a contribution from microbial biomass consisting of
575 methanotrophic archaea and sulphate reducing bacteria rather than from terrestrial organic carbon that has an
576 average $\delta^{13}C$-value of -27‰ (e.g. Rachold and Hubberten, 1999). This is also supported by the Corg/Ntot
577 values, which do not show excursions to higher values where $\delta^{13}C$ -TOC values are low (Fig. 6), which would be
578 expected from terrestrial organic carbon. We assume our $\delta^{13}C$ -TOC values to represent mixing between marine

organic matter (i.e. primary production) and methanotrophic/chemosynthetic biomass which seem to have similar Corg/Ntot ratios, but large differences in $\delta^{13}C$ values. All push cores, except for the non-seep core, showed strong decrease in $\delta^{13}C$-TOC with depth, which is interpreted as an increasing proportion of methanotrophic biomass with depth. PC009 with the lowest $\delta^{13}C$-TOC values presumably contains the highest proportion of methanotrophic biomass. Also, PC021 shows a pronounced decrease in $\delta^{13}C$ -TOC from around 14 cm (-23.4‰) to 38 cm (-30.7‰). When compared with our lipid biomarker data, from 17 cm and downward, an increasing trend in archaeol content and a decreasing trend in $\delta^{13}C$-archaeol and $\delta^{13}C$-sn2-hydroxyarchaeol can be deduced (Fig.11). This pattern agrees well with the decreasing trend of $\delta^{13}C$ of the TOC pool and confirms that this is caused by the presence of methanotrophic microbial biomass. There is another interval further towards the top of PC021 (c. 8 cmbsf) with elevated archaeol content and relatively lower $\delta^{13}C$ values of both archaeol and sn2-hydroxyarchaeol. This could indicate SMT fluctuations as marked by the grey intervals in Fig. 11. Another possibility could be a situation similar to the double SMT observed offshore north-western Svalbard by Treude et al. (2020). The authors suggest non-vertical methane transport causing a second interval with an activity maximum of sulphate dependent AOM.

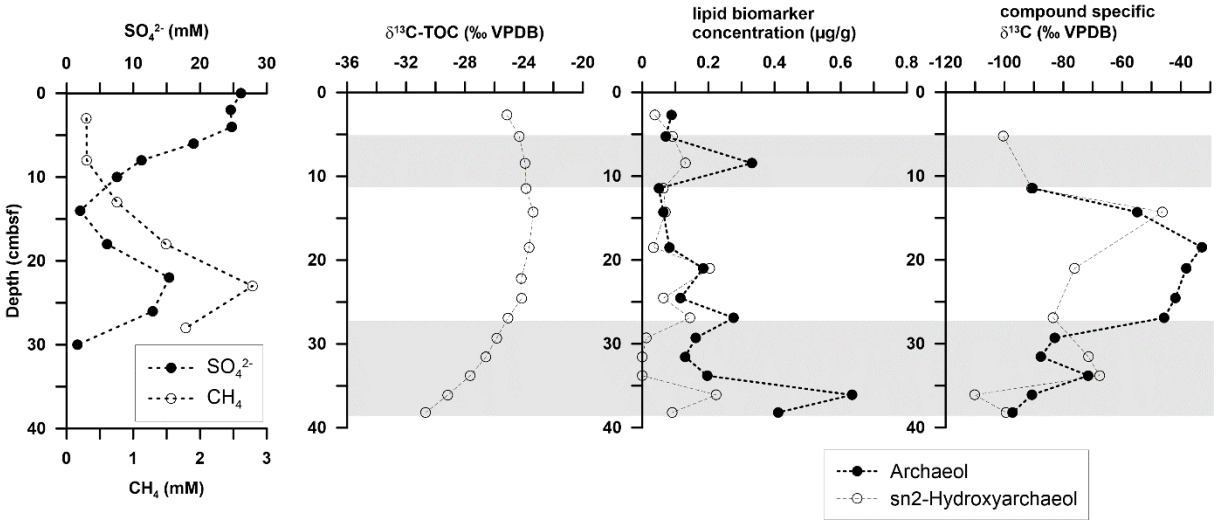

Figure 11:from left to right: pore water sulphate and methane concentration in PC021, the $\delta^{13}C$ of total organic carbon (TOC) in PC021, and the content and compound specific $\delta^{13}C$ of the lipid biomarkers archaeol and sn2-hydroxyarchaeol. The grey bands represent intervals with elevated content of archaeol and relatively low values of $\delta^{13}C$ of both archaeol and sn2-hydroxyarchaeol.

To determine whether the decrease in $\delta^{13}C$-TOC in our seep push cores can be explained by the incorporation of ^{13}C depleted carbon from methane or DIC during AOM we included -organic carbon formation in our transport-reaction-model (see reaction rate R-POC formation in Fig 10). Previous studies show that ANME can assimilate carbon from both methane and DIC (Kellermann et al., 2012; Wegener et al., 2008), and that usually very low amounts of carbon are assimilated compared to amounts of methane oxidised (e.g. around 1 mol% ,Wegener et.,

al 2008). The result of our modelling exercise for PC017 shows that the highest rate of organic carbon formation occurs at around 12 cm, very close to the SMT, where AOM rates are highest (Fig. 10). However, the lowest δ^{13}C-TOC values in PC017 are found at the bottom of the core at 38 cmbsf. We consider two different options to explain this discrepancy. In the first option, the SMT with the highest rates of AOM and carbon assimilation by the AOM-performing microbial community might have been situated further down in the sedimentary column previously. The fact that δ^{13}C-TOC values in all push cores, except the non-seep core (PC020), are lowest below the present-day SMT supports this explanation and indicates a lower methane flux in both Lunde and Lomvi pockmark in the past. For the second option, both the low δ^{13}C-TOC values and the seep carbonates in PC009 below the present-day SMT could, on the other hand, also be explained by a higher methane flux in the past. When these sediment layers were situated near the sediment surface under higher flux conditions this would have resulted in the accumulation of ^{13}C-depleted TOC and aragonite- and Mg-calcite-dominated seep carbonates close to the sediment water interface. A subsequent burial to grater depths (where they are found now) and a lowering in the methane flux could explain the absence of seep carbonates in our push cores close to the sediment surface and δ^{13}C-TOC values closer to background values at the top of the cores (Fig. 6).

No matter whether an increase or a decrease in methane flux was responsible for the geochemical patterns in our push cores, from our data set we cannot ascertain the reason for a change in fluid flow. However, cold seeps are known to show very dynamic fluid escape patterns. Previous studies suggest that the regional stress regime is the main external factor controlling the long-term pattern of gas seepage at the Vestnesa Ridge (Plaza-Faverola and Keiding, 2019). Shorter-term changes in fluid flow might be due to local gas hydrate destabilization caused by ascending warmer fluids, changing fluid pathways due to local clogging of fractures by gas-hydrates or seep carbonates (e.g. Himmler et al., 2019; Luff et al., 2004), or by the formation of new fractures (Treude et al., 2020; Yao et al., 2019)

7.3 Microbial methanogenesis fuelled by thermogenic hydrocarbon-sustained biomass

The large variability in δ^{13}C-CH_4 values in our cores is probably the result of the mixing of different proportions of thermogenic and microbial methane and the influence of AOM. The effect of methane oxidation was especially visible in PC020 where methane concentrations in the sediments were low throughout the core (<9 µM.). This methane represents the residual after oxidation and is thus enriched in ^{13}C compared to methane sampled below the SMT, which has not been strongly affected by oxidation yet. PC017 showed the lowest δ^{13}C-CH_4 values between -77.4‰ and -73.3‰ indicating the highest proportion of microbial methane (Whiticar, 1999). Combining carbon and hydrogen isotopic data of methane (Fig. 4B), can help interpret the methane

source (Whiticar, 1999). All our samples from cores PC009, PC017 and PC021 plot in the field of hydrogenotrophic methanogenesis (CO_2 reduction), which is the process of methanogenic archaea growing on carbon dioxide and using H_2 as a source of electrons to reduce CO_2 (Richards et al., 2016). Four samples from PC021 plot close to the mixing field of microbial and thermogenic methane but these samples might be affected by methane oxidation, which increases the $\delta^{13}C\text{-}CH_4$ value (as indicated by the arrow in Fig. 4B). Although methane isotopes seem to indicate a microbial origin, $\delta^{13}C\text{-}C_2H_6$ values are well within the thermogenic range (Fig. 5). The plot of $\delta^{13}C\text{-}C_2H_6$ vs. $\delta^{13}C\text{-}CH_4$ values shows that gas samples of known microbial origin show $\delta^{13}C\text{-}C_2H_6$ values mostly below -60‰ (Nakagawa et al., 2003), more than 30‰ lower than in the Vestnesa push core samples.

There is evidence supporting the hypothesis that the gas hydrate system and large-scale fluid migration at Vestnesa Ridge is fuelled by deep thermogenic hydrocarbons. The gas analyses of gas hydrate samples show exclusively thermogenic signatures (Graves et al., 2017; Panieri et al., 2017; Pape et al., 2020; Plaza-Faverola et al., 2017; Smith et al., 2014)(Fig. 4). Seismic chimneys, consisting of vertical zones of disrupted reflections, connect to active pockmarks and are rooted in the free gas zone below the BSR (Hustoft et al., 2009). The location of the chimneys and pockmarks on the crest correlates with the location of the BSR anticline and is also related to the occurrence of fault planes which can facilitate fluid migration (Hustoft et al., 2009; Plaza-Faverola et al., 2015). Hydrocarbon migration modelling suggests large scale fluid migration started around 6 million years ago and reached the seafloor around 2 million years ago (Knies et al., 2018). Miocene source rock observed in ODP Hole 909 and inferred below Hole 909 (Knies and Mann, 2002; Stein et al., 1995) have been suggested to fuel the gas hydrate system at Vestnesa Ridge since then. This is also discussed in detail by Pape et al. (2020) who show that thermogenic hydrocarbons dominate the gas signature at the seep sites including the gas hydrate samples and point towards a common deep-hydrocarbon source for both Lunde and Lomvi pockmark. On the other hand, shallow gas samples from our push cores in Lunde and Lomvi pockmark sampled at seep locations show a strong signal of microbial methane which had not been observed from Vestnesa Ridge yet. We suggest two possible ways to explain this: (1) microbial methanogenesis in shallow sediment as a result of organic matter degradation fuelled by methane-seep related biomass or (2) secondary methanogenesis as a result of thermogenic hydrocarbon biodegradation (e.g. Milkov, 2011; Mishra et al., 2017; Stagars et al., 2017). Some admixture of thermogenic gas in our samples is evident from the high ethane $\delta^{13}C$ values (Fig. 5). But due to a lack of $\delta^{13}C$ measurements of higher hydrocarbons it is at this stage not possible to conclude on possible biodegradation of the higher hydrocarbons. In both scenarios of microbial methane formation, the thermogenic

hydrocarbon seepage is a prerequisite to produce microbial methane in the shallow subsurface sediments, either through providing higher hydrocarbons for biodegradation, or providing seep habitats that induce accumulation of organic matter. The pockmarks are a result of large-scale hydrocarbon migration and produce methane seeps that are a biological oasis on the high Arctic seafloor. For example, seep carbonates can enhance the occurrence of fauna, because they provide sites for aggregation. Also fractures or pockets in the sediment often provide space and nutrients for microbial habitats that create a favourable condition for higher biomass accumulation such as biofilms (Briggs et al., 2011; Gründger et al., 2019). A study by Åström et al. (2018) shows that the infaunal biomass is 5 times higher at the Vestnesa pockmarks than at a high Arctic deep-sea control site. Furthermore, our sedimentary organic matter analyses suggest considerable methanotrophic biomass in the sediment. Another prerequisite for microbial methanogenesis is low sulphate concentrations. Sulphate is removed rapidly in shallow sediments due to sulphate dependent AOM as shown by our pore water profiles. The high supply of organic matter and the low concentrations of pore water sulphate can thus facilitate microbial methanogenesis (e.g. Paulo et al., 2015, and references therein), which shows that this can only occur as a result of the thermogenic hydrocarbon migration. This is supported by the fact that in our non-seep core PC020, which showed no seep indications, there is no shallow microbial methane detected, although TOC content is relatively high.

8 Conclusions

1. Pore water profiles from seep sites within Lunde and Lomvi pockmark show numerous indications of anaerobic oxidation of methane occurring in shallow subsurface sediments, such as rapid sulphate depletion, strong increase in alkalinity and low δ^{13}C-DIC values. The depth profiles of δ^{13}C-DIC and alkalinity, combined with transport reaction modelling suggest advective aqueous fluid transport assists the escape of methane from the Lunde pockmark sediments. This results in considerable flux of dissolved methane across the sediment-water interface not previously reported from Vestnesa Ridge and highlights the value of video guided sampling of seep sites which had not been done at Vestnesa Ridge previously.

2. The depth profiles of δ^{13}C-TOC and lipid biomarker data indicate a significant amount of AOM-associated microbial biomass in our sediment cores that do not correspond to the present-day sulphate-methane transition. The negative trends in δ^{13}C-TOC and the occurrence of seep carbonates below the present-day SMT could be explained either by a previously deeper SMT in the sediment and thus a lower methane flux in the past, or by a previously higher methane flux creating strong ^{13}C-depletion in the TOC and seep carbonate accumulation in near-surface sediments which were subsequently buried to deeper depths preserving the SMT-signature.

3. The large-scale fluid flow and gas-hydrate system at Vestnesa Ridge is fuelled by deep thermogenic hydrocarbons and we observed a clear thermogenic signature in the $\delta^{13}C$ of ethane gas in our push cores. However, distinct signals of microbial methane in the shallow subseafloor sediments are also evident from our push cores. We link this to microbial methanogenesis which is sustained only by the occurrence of the seeps that provide habitats for the increased production of biomass (the basis for methanogenesis), compared to the 'background' Arctic seafloor where organic carbon content is lower and no methane is found in the shallow subsurface.

9 Acknowledgements

We would like to acknowledge the crew and chief scientist of cruise "G.O. Sars" cruise P1606, and the team handling the ROV Ægir. We are grateful to Serge Robert for support during CH_4 measurements and for $\delta^{13}C$-DIC measurements at EAWAG. We want to thank Jasmin Schönenberger and Tonu Martma for XRD and $\delta^{13}C$-carbonate analyses, respectively. Thanks to the constructive comments of the reviewers this manuscript was improved compared to previous versions.

This study was funded by the Research Council of Norway through its Centres of Excellence funding scheme grant 287 no. 223259 (CAGE), and by the project Petromaks2 NORCRUST – Norwegian Margin Fluid Systems and Methane-derived Authigenic carbonate Crusts (project #255150).

10 References

Aloisi, G., Bouloubassi, I., Heijs, S.K., Pancost, R.D., Pierre, C., Sinninghe Damsté, J.S., Gottschal, J.C., Forney, L.J., Rouchy, J.-M., 2002. CH4-consuming microorganisms and the formation of carbonate crusts at cold seeps. Earth and Planetary Science Letters, 203(1): 195-203.http://dx.doi.org/10.1016/S0012-821X(02)00878-6

Ambrose, W.G., Panieri, G., Schneider, A., Plaza-Faverola, A., Carroll, M.L., Åström, E.K.L., Locke, W.L., Carroll, J., 2015. Bivalve shell horizons in seafloor pockmarks of the last glacial-interglacial transition: a thousand years of methane emissions in the Arctic Ocean. Geochemistry, Geophysics, Geosystems, 16(12): 4108-4129.https://doi.org/10.1002/2015GC005980

Andreassen, K., Hubbard, A., Winsborrow, M., Patton, H., Vadakkepuliyambatta, S., Plaza-Faverola, A., Gudlaugsson, E., Serov, P., Deryabin, A., Mattingsdal, R., Mienert, J., Bünz, S., 2017. Massive blow-out craters formed by hydrate-controlled methane expulsion from the Arctic seafloor. Science, 356(6341): 948-953.https://doi.org/10.1126/science.aal4500

Åström, E.K.L., Carroll, M.L., Ambrose Jr., W.G., Sen, A., Silyakova, A., Carroll, J., 2018. Methane cold seeps as biological oases in the high-Arctic deep sea. Limnology and Oceanography, 63(S1): S209-S231.https://doi.org/10.1002/lno.10732

Bayon, G., Henderson, G.M., Bohn, M., 2009. U–Th stratigraphy of a cold seep carbonate crust. Chemical Geology, 260(1–2): 47-56.http://dx.doi.org/10.1016/j.chemgeo.2008.11.020

Bian, Y., Feng, D., Roberts, H.H., Chen, D., 2013. Tracing the evolution of seep fluids from authigenic carbonates: Green Canyon, northern Gulf of Mexico. Marine and Petroleum Geology, 44: 71-81.http://dx.doi.org/10.1016/j.marpetgeo.2013.03.010

Boetius, A., Ravenschlag, K., Schubert, C.J., Rickert, D., Widdel, F., Gieseke, A., Amann, R., Jorgensen, B.B., Witte, U., Pfannkuche, O., 2000. A marine microbial consortium apparently mediating anaerobic oxidation of methane. Nature, 407(6804): 623-626.http://www.nature.com/nature/journal/v407/n6804/suppinfo/407623a0_S1.html

Boudreau, B., 1997. Diagenetic models and their implementation: modelling transport and reactions in aquatic sediments. Springer, Berlin, Heidelberg, NY, 414 pp

Briggs, B.R., Pohlman, J.W., Torres, M., Riedel, M., Brodie, E.L., Colwell, F.S., 2011. Macroscopic Biofilms in Fracture-Dominated Sediment That Anaerobically Oxidize Methane. Applied and Environmental Microbiology, 77(19): 6780-6787.http://dx.doi.org/10.1128/aem.00288-11

Bünz, S., Polyanov, S., Vadakkepuliyambatta, S., Consolaro, C., Mienert, J., 2012. Active gas venting through hydrate-bearing sediments on the Vestnesa Ridge, offshore W-Svalbard. Marine Geology, 332–334(0): 189-197.http://dx.doi.org/10.1016/j.margeo.2012.09.012

Collins, P.F., Diehl, H., Smith, G.F., 1959. 2,4,6-Tripyridyl-s-triazine as Reagent for Iron. Determination of Iron in Limestone, Silicates, and Refractories. Analytical Chemistry, 31(11): 1862-1867.http://dx.doi.org/10.1021/ac60155a056

Dekkers, M.J., 1978. Magnetic properties of sediments, Sedimentology. Springer Berlin Heidelberg, Berlin, Heidelberg, pp. 684-692.http://dx.doi.org/10.1007/3-540-31079-7_130

Dessandier, P.-A., Borrelli, C., Yao, H., Sauer, S., Hong, W.-L., Panieri, G., 2020. Foraminiferal δ18O reveals gas hydrate dissociation in Arctic and North Atlantic ocean sediments. Geo-Marine Letters.http://dx.doi.org/10.1007/s00367-019-00635-6

Egger, M., Riedinger, N., Mogollón, J.M., Jørgensen, B.B., 2018. Global diffusive fluxes of methane in marine sediments. Nature Geoscience, 11(6): 421-425.http://dx.doi.org/10.1038/s41561-018-0122-8

Eiken, O., Hinz, K., 1993. Contourites in the Fram Strait. Sedimentary Geology, 82(1): 15-32.https://doi.org/10.1016/0037-0738(93)90110-Q

Engen, Ø., Faleide, J.I., Dyreng, T.K., 2008. Opening of the Fram Strait gateway: A review of plate tectonic constraints. Tectonophysics, 450(1): 51-69.https://doi.org/10.1016/j.tecto.2008.01.002

EPA, 1983. 600/4-79-020 Methods for Chemical Analysis of Water and Wastes United States Environmental Protection Agency (US EPA) Criteria, pp. http://www.wbdg.org/ffc/epa/criteria/epa-600-4-79-020

Ferré, B., Jansson, P.G., Moser, M., Serov, P., Portnov, A., Graves, C.A., Panieri, G., Gründger, F., Berndt, C., Lehmann, M.F., Niemann, H., 2020. Reduced methane seepage from Arctic sediments during cold bottom-water conditions. Nature Geoscience, 13(2): 144-148.https://doi.org/10.1038/s41561-019-0515-3

Froelich, P.N., Klinkhammer, G.P., Bender, M.L., Luedtke, N.A., Heath, G.R., Cullen, D., Dauphin, P., Hammond, D., Hartman, B., Maynard, V., 1979. Early oxidation of organic matter in pelagic sediments of the eastern equatorial Atlantic: suboxic

diagenesis. Geochimica et Cosmochimica Acta, 43(7): 1075-1090.http://dx.doi.org/10.1016/0016-7037(79)90095-4

Gieskes, J., Mahn, C., Day, S., Martin, J.B., Greinert, J., Rathburn, T., McAdoo, B., 2005. A study of the chemistry of pore fluids and authigenic carbonates in methane seep environments: Kodiak Trench, Hydrate Ridge, Monterey Bay, and Eel River Basin. Chemical Geology, 220(3–4): 329-345.http://dx.doi.org/10.1016/j.chemgeo.2005.04.002

Goswami, B.K., Weitemeyer, K.A., Minshull, T.A., Sinha, M.C., Westbrook, G.K., Chabert, A., Henstock, T.J., Ker, S., 2015. A joint electromagnetic and seismic study of an active pockmark within the hydrate stability field at the Vestnesa Ridge, West Svalbard margin. Journal of Geophysical Research: Solid Earth, 120(10): 6797-6822.10.1002/2015jb012344

Graves, C.A., James, R.H., Sapart, C.J., Stott, A.W., Wright, I.C., Berndt, C., Westbrook, G.K., Connelly, D.P., 2017. Methane in shallow subsurface sediments at the landward limit of the gas hydrate stability zone offshore western Svalbard. Geochimica et Cosmochimica Acta, 198: 419-438.https://doi.org/10.1016/j.gca.2016.11.015

Gründger, F., Carrier, V., Svenning, M.M., Panieri, G., Vonnahme, T.R., Klasek, S., Niemann, H., 2019. Methane-fuelled biofilms predominantly composed of methanotrophic ANME-1 in Arctic gas hydrate-related sediments. Scientific Reports, 9: 9725.https://doi.org/10.1038/s41598-019-46209-5

Haese, R.R., Meile, C., Van Cappellen, P., De Lange, G.J., 2003. Carbon geochemistry of cold seeps: Methane fluxes and transformation in sediments from Kazan mud volcano, eastern Mediterranean Sea. Earth and Planetary Science Letters, 212(3): 361-375.https://doi.org/10.1016/S0012-821X(03)00226-7

Himmler, T., Sahy, D., Martma, T., Bohrmann, G., Plaza-Faverola, A., Bunz, S., Condon, D.J., Knies, J., Lepland, A., 2019. A 160,000-year-old history of tectonically controlled methane seepage in the Arctic. Sci Adv, 5(8): eaaw1450.https://doi.org/10.1126/sciadv.aaw1450

Hinrichs, K.-U., Hayes, J.M., Sylva, S.P., Brewer, P.G., DeLong, E.F., 1999. Methane-consuming archaebacteria in marine sediments. Nature, 398(6730): 802-805.https://doi.org/10.1038/19751

Hong, W.-L., Latour, P., Sauer, S., Sen, A., Gilhooly, W.P., Lepland, A., Fouskas, F., 2020. Iron cycling in Arctic methane seeps. Geo-Marine Letters.https://doi.org/10.1007/s00367-020-00649-5

Hong, W.-L., Sauer, S., Panieri, G., Ambrose, W.G., James, R.H., Plaza-Faverola, A., Schneider, A., 2016. Removal of methane through hydrological, microbial, and geochemical processes in the shallow sediments of pockmarks along eastern Vestnesa Ridge (Svalbard). Limnology and Oceanography.https://doi.org/10.1002/lno.10299

Hong, W.-L., Torres, M.E., Kim, J.-H., Choi, J., Bahk, J.-J., 2014. Towards quantifying the reaction network around the sulfate–methane-transition-zone in the Ulleung Basin, East Sea, with a kinetic modeling approach. Geochimica et Cosmochimica Acta, 140: 127-141.http://dx.doi.org/10.1016/j.gca.2014.05.032

Hong, W.L., Torres, M.E., Carroll, J., Cremiere, A., Panieri, G., Yao, H., Serov, P., 2017. Seepage from an arctic shallow marine gas hydrate reservoir is insensitive to momentary ocean warming. Nat Commun, 8: 15745.https://doi.org/10.1038/ncomms15745

Hong, W.L., Torres, M.E., Portnov, A., Waage, M., Haley, B., Lepland, A., 2018. Variations in Gas and Water Pulses at an Arctic Seep: Fluid Sources and Methane Transport. Geophysical Research Letters.https://doi.org/10.1029/2018gl077309

Howe, J.A., Shimmield, T.M., Harland, R., Eyles, N., 2008. Late Quaternary contourites and glaciomarine sedimentation in the Fram Strait. Sedimentology, 55(1): 179-200.https://doi.org/10.1111/j.1365-3091.2007.00897.x

Hustoft, S., Bünz, S., Mienert, J., Chand, S., 2009. Gas hydrate reservoir and active methane-venting province in sediments on < 20 Ma young oceanic crust in the Fram Strait, offshore NW-Svalbard. Earth and Planetary Science Letters, 284(1–2): 12-24.http://dx.doi.org/10.1016/j.epsl.2009.03.038

IPCC, 2019. Climate Change and Land: an IPCC special report on climate change, desertification, land degradation, sustainable land management, food security, and greenhouse gas fluxes in terrestrial ecosystems

Iversen, N., Jørgensen, B.B., 1985. Anaerobic methane oxidation rates at the sulfate-methane transition in marine sediments from Kattegat and Skagerrak (Denmark) 1. Limnology and Oceanography, 30(5): 944-955.https://doi.org/10.4319/lo.1985.30.5.0944

Jakobsson, M., Mayer, L., Coakley, B., Dowdeswell, J.A., Forbes, S., Fridman, B., Hodnesdal, H., Noormets, R., Pedersen, R., Rebesco, M., Schenke, H.W., Zarayskaya, Y., Accettella, D., Armstrong, A., Anderson, R.M., Bienhoff, P., Camerlenghi, A., Church, I., Edwards, M., Gardner, J.V., Hall, J.K., Hell, B., Hestvik, O., Kristoffersen, Y., Marcussen, C., Mohammad, R., Mosher, D., Nghiem, S.V., Pedrosa, M.T., Travaglini, P.G., Weatherall, P., 2012. The International Bathymetric Chart of the Arctic Ocean (IBCAO) Version 3.0. Geophysical Research Letters, 39(12): n/a-n/a.https://doi.org/10.1029/2012gl052219

Jansson, P., Triest, J., Grilli, R., Ferré, B., Silyakova, A., Mienert, J., Chappellaz, J., 2019. High-resolution underwater laser spectrometer sensing provides new insights into methane distribution at an Arctic seepage site. Ocean Sci., 15(4): 1055-1069.https://doi.org/10.5194/os-15-1055-2019

Judd, A.G., Hovland, M., 2007. Seabed fluid flow. Cambridge University Press, New York

Katz, B.J., Narimanov, A., Huseinzadeh, R., 2002. Significance of microbial processes in gases of the South Caspian basin. Marine and Petroleum Geology, 19(6): 783-796.http://dx.doi.org/10.1016/S0264-8172(02)00086-7

Kellermann, M.Y., Wegener, G., Elvert, M., Yoshinaga, M.Y., Lin, Y.S., Holler, T., Mollar, X.P., Knittel, K., Hinrichs, K.U., 2012. Autotrophy as a predominant mode of carbon fixation in anaerobic methane-oxidizing microbial communities. Proc Natl Acad Sci U S A, 109(47): 19321-6.https://doi.org/10.1073/pnas.1208795109

Kenna, T.C., Nitsche, F.O., Herron, M.M., Mailloux, B.J., Peteet, D., Sritrairat, S., Sands, E., Baumgarten, J., 2011. Evaluation and calibration of a Field Portable X-Ray Fluorescence spectrometer for quantitative analysis of siliciclastic soils and sediments. Journal of Analytical Atomic Spectrometry, 26(2): 395-405

Klasek, S., Torres, M.E., Bartlett, D.H., Tyler, M., Hong, W.-L., Colwell, F., 2020. Microbial communities from Arctic marine sediments respond slowly to methane addition during ex situ enrichments. Environmental Microbiology, 22(5): 1829-1846.https://doi.org/10.1111/1462-2920.14895

Knies, J., Daszinnies, M., Plaza-Faverola, A., Chand, S., Sylta, Ø., Bünz, S., Johnson, J.E., Mattingsdal, R., Mienert, J., 2018. Modelling persistent methane seepage offshore western Svalbard since early Pleistocene. Marine and Petroleum Geology.https://doi.org/10.1016/j.marpetgeo.2018.01.020

Knies, J., Mann, U., 2002. Depositional environment and source rock potential of Miocene strata from the central Fram Strait: introduction of a new computing tool for simulating organic facies variations. Marine and Petroleum Geology, 19(7): 811-828.https://doi.org/10.1016/S0264-8172(02)00090-9

Luff, R., Wallmann, K., 2003. Fluid flow, methane fluxes, carbonate precipitation and biogeochemical turnover in gas hydrate-bearing sediments at Hydrate Ridge, Cascadia

Margin: numerical modeling and mass balances. Geochimica et Cosmochimica Acta, 67(18): 3403-3421.http://dx.doi.org/10.1016/S0016-7037(03)00127-3
Luff, R., Wallmann, K., Aloisi, G., 2004. Numerical modeling of carbonate crust formation at cold vent sites: significance for fluid and methane budgets and chemosynthetic biological communities. Earth and Planetary Science Letters, 221(1–4): 337-353.http://dx.doi.org/10.1016/S0012-821X(04)00107-4
MacDonald, I.R., Leifer, I., Sassen, R., Stine, P., Mitchell, R., Guinasso, N., 2002. Transfer of hydrocarbons from natural seeps to the water column and atmosphere. Geofluids, 2(2): 95-107.https://doi.org/10.1046/j.1468-8123.2002.00023.x
Milkov, A.V., 2011. Worldwide distribution and significance of secondary microbial methane formed during petroleum biodegradation in conventional reservoirs. Organic Geochemistry, 42(2): 184-207.http://dx.doi.org/10.1016/j.orggeochem.2010.12.003
Mishra, S., Wefers, P., Schmidt, M., Knittel, K., Krüger, M., Stagars, M.H., Treude, T., 2017. Hydrocarbon Degradation in Caspian Sea Sediment Cores Subjected to Simulated Petroleum Seepage in a Newly Designed Sediment-Oil-Flow-Through System. Frontiers in Microbiology, 8(763).https://doi.org/10.3389/fmicb.2017.00763
Myhre, C.L., Ferré, B., Platt, S.M., Silyakova, A., Hermansen, O., Allen, G., Pisso, I., Schmidbauer, N., Stohl, A., Pitt, J., Jansson, P., Greinert, J., Percival, C., Fjaeraa, A.M., O'Shea, S.J., Gallagher, M., Le Breton, M., Bower, K.N., Bauguitte, S.J.B., Dalsøren, S., Vadakkepuliyambatta, S., Fisher, R.E., Nisbet, E.G., Lowry, D., Myhre, G., Pyle, J.A., Cain, M., Mienert, J., 2016. Extensive release of methane from Arctic seabed west of Svalbard during summer 2014 does not influence the atmosphere. Geophysical Research Letters: n/a-n/a.https://doi.org/10.1002/2016GL068999
Nakagawa, F., Tsunogai, U., Yoshida, N., Adams, D.D., 2003. 8 - Stable isotopic compositions of bacterial light hydrocarbons in marginal marine sediments. In: Taniguchi, M.T.W.G., Wang, K., Gamo, T. (Eds.), Land and Marine Hydrogeology. Elsevier, Amsterdam, pp. 141-150.http://dx.doi.org/10.1016/B978-044451479-0/50021-2
Niemann, H., Elvert, M., 2008. Diagnostic lipid biomarker and stable carbon isotope signatures of microbial communities mediating the anaerobic oxidation of methane with sulphate. Organic Geochemistry, 39(12): 1668-1677.https://doi.org/10.1016/j.orggeochem.2007.11.003
Panieri, G., Bünz, S., Fornari, D.J., Escartin, J., Serov, P., Jansson, P., Torres, M.E., Johnson, J.E., Hong, W., Sauer, S., Garcia, R., Gracias, N., 2017. An integrated view of the methane system in the pockmarks at Vestnesa Ridge, 79°N. Marine Geology, 390: 282-300.https://doi.org/10.1016/j.margeo.2017.06.006
Panieri, G., Lepland, A., Whitehouse, M.J., Wirth, R., Raanes, M.P., James, R.H., Graves, C.A., Crémière, A., Schneider, A., 2016. Diagenetic Mg-calcite overgrowths on foraminiferal tests in the vicinity of methane seeps. Earth and Planetary Science Letters.https://doi.org/10.1016/j.epsl.2016.10.024
Pape, T., Bünz, S., Hong, W.-L., Torres, M.E., Riedel, M., Panieri, G., Lepland, A., Hsu, C.-W., Wintersteller, P., Wallmann, K., Schmidt, C., Yao, H., Bohrmann, G., 2020. Origin and Transformation of Light Hydrocarbons Ascending at an Active Pockmark on Vestnesa Ridge, Arctic Ocean. Journal of Geophysical Research: Solid Earth, 125(1): e2018JB016679.https://doi.org/10.1029/2018jb016679
Paull, C.K., Lorenson, T.D., Borowski, W.S., Ussler, W., III, Olsen, K., Rodriguez, N.M., 2000. Isotopic composition of CH4, CO2 species, and sedimentary organic matter within samples from the Blake Ridge: gas source implications. In: Paull, C.K., Matsumoto, R., Wallace, P.J., Dillon, W.P. (Eds.), Proc. ODP, Sci. Results, 164, College Station, TX (Ocean Drilling Program), pp. 67-78.http://www-odp.tamu.edu/publications/164_SR/chap_07/ch7_.htm

927 Paulo, L.M., Stams, A.J.M., Sousa, D.Z., 2015. Methanogens, sulphate and heavy metals: a
928 complex system. Reviews in Environmental Science and Bio/Technology, 14(4): 537-
929 553.10.1007/s11157-015-9387-1
930 Plaza-Faverola, A., Bünz, S., Johnson, J.E., Chand, S., Knies, J., Mienert, J., Franek, P., 2015.
931 Role of tectonic stress in seepage evolution along the gas hydrate-charged Vestnesa
932 Ridge, Fram Strait. Geophysical Research Letters, 42(3): 733-
933 742.https://doi.org/10.1002/2014gl062474
934 Plaza-Faverola, A., Keiding, M., 2019. Correlation between tectonic stress regimes and
935 methane seepage on the western Svalbard margin. Solid Earth, 10(1): 79-
936 94.https://doi.org/10.5194/se-10-79-2019
937 Plaza-Faverola, A., Vadakkepuliyambatta, S., Hong, W.-L., Mienert, J., Bünz, S., Chand, S.,
938 Greinert, J., 2017. Bottom-simulating reflector dynamics at Arctic thermogenic gas
939 provinces: An example from Vestnesa Ridge, offshore west Svalbard. Journal of
940 Geophysical Research: Solid Earth, 122(6): 4089-
941 4105.https://doi.org/10.1002/2016jb013761
942 Puglini, M., Brovkin, V., Regnier, P., Arndt, S., 2019. Assessing the potential for non-
943 turbulent methane escape from the East Siberian Arctic Shelf. Biogeosciences
944 Discussions: 1-44.https://doi.org/10.5194/bg-2019-264
945 Rachold, V., Hubberten, H.W., 1999. Carbon Isotope Composition of Particulate Organic
946 Material in East Siberian Rivers. In: al., K.H.e. (Ed.), Land-Ocean Systems in the
947 Siberian Arctic. Springer, Berlin, Heidelberg.https://doi.org/10.1007/978-3-642-
948 60134-7_21
949 Reeburgh, W.S., 2003. Global methane biogeochemistry. In: Keeling, R.F., Holland, H.D.,
950 Turekian, K.K. (Eds.), Treatise on Geochemistry, Vol. 4: The Atmosphere.
951 UK:Elsevier-Pergamon, Oxford, pp. 65-89.https://doi.org/10.1016/B0-08-043751-
952 6/04036-6
953 Rees, C.E., 1973. A steady-state model for sulphur isotope fractionation in bacterial reduction
954 processes. Geochimica et Cosmochimica Acta, 37(5): 1141-
955 1162.https://doi.org/10.1016/0016-7037(73)90052-5
956 Richards, M.A., Lie, T.J., Zhang, J., Ragsdale, S.W., Leigh, J.A., Price, N.D., 2016.
957 Exploring Hydrogenotrophic Methanogenesis: a Genome Scale Metabolic
958 Reconstruction of Methanococcus maripaludis. Journal of Bacteriology, 198(24):
959 3379-3390.https://doi.org/10.1128/jb.00571-16
960 Sauer, S., Crémière, A., Knies, J., Lepland, A., Sahy, D., Martma, T., Noble, S.R.,
961 Schönenberger, J., Klug, M., Schubert, C.J., 2017. U-Th chronology and formation
962 controls of methane-derived authigenic carbonates from the Hola trough seep area,
963 northern Norway. Chemical Geology, 470: 164-
964 179.https://doi.org/10.1016/j.chemgeo.2017.09.004
965 Sauer, S., Hong, W.-L., Knies, J., Lepland, A., Forwick, M., Klug, M., Eichinger, F.,
966 Baranwal, S., Crémière, A., Chand, S., Schubert, C.J., 2016. Sources and turnover of
967 organic carbon and methane in fjord and shelf sediments off northern Norway.
968 Geochemistry, Geophysics, Geosystems, 17(10): 4011-
969 4031.https://doi.org/10.1002/2016GC006296
970 Sauer, S., Knies, J., Lepland, A., Chand, S., Eichinger, F., Schubert, C.J., 2015. Hydrocarbon
971 sources of cold seeps off the Vesterålen coast, northern Norway. Chemical Geology,
972 417: 371-382.http://dx.doi.org/10.1016/j.chemgeo.2015.10.025
973 Schneider, A., Panieri, G., Lepland, A., Consolaro, C., Crémière, A., Forwick, M., Johnson,
974 J.E., Plaza-Faverola, A., Sauer, S., Knies, J., 2018. Methane seepage at Vestnesa
975 Ridge (NW Svalbard) since the Last Glacial Maximum. Quaternary Science Reviews,
976 193: 98-117.https://doi.org/10.1016/j.quascirev.2018.06.006

977 Schwertmann, U., Fitzpatrick, R.W., 1992. Iron minerals in surface environments. In:
978 Skinner, H.C.W., Fitzpatrick, R.W. (Eds.), Biomineralization Processes of Iron and
979 Manganese: Modern and Ancient Environments. Catena Verlag, pp. 7-
980 30.http://dx.doi.org/10.1086/629741
981 Seeberg-Elverfeldt, J., Schlüter, M., Feseker, T., Kölling, M., 2005. Rhizon sampling of
982 porewaters near the sediment-water interface of aquatic systems. Limnology and
983 Oceanography: Methods, 3(8): 361-371.https://doi.org/10.4319/lom.2005.3.361
984 Shakhova, N., Semiletov, I., Leifer, I., Salyuk, A., Rekant, P., Kosmach, D., 2010.
985 Geochemical and geophysical evidence of methane release over the East Siberian
986 Arctic Shelf. Journal of Geophysical Research: Oceans, 115(C8): n/a-
987 n/a.https://doi.org/10.1029/2009JC005602
988 Silyakova, A., Jansson, P., Serov, P., Ferré, B., Pavlov, A.K., Hattermann, T., Graves, C.A.,
989 Platt, S.M., Myhre, C.L., Gründger, F., Niemann, H., 2020. Physical controls of
990 dynamics of methane venting from a shallow seep area west of Svalbard. Continental
991 Shelf Research, 194: 104030.https://doi.org/10.1016/j.csr.2019.104030
992 Smith, A.J., Mienert, J., Bünz, S., Greinert, J., 2014. Thermogenic methane injection via
993 bubble transport into the upper Arctic Ocean from the hydrate-charged Vestnesa
994 Ridge, Svalbard. Geochemistry, Geophysics, Geosystems, 15(5): 1945-
995 1959.https://doi.org/10.1002/2013GC005179
996 Stagars, M.H., Mishra, S., Treude, T., Amann, R., Knittel, K., 2017. Microbial Community
997 Response to Simulated Petroleum Seepage in Caspian Sea Sediments. Frontiers in
998 Microbiology, 8(764).https://doi.org/10.3389/fmicb.2017.00764
999 Stein, R., Brass, G., Graham, D., Pimmel, A., 1995. Hydrocarbon measurements at Arctic
1000 gateways sites (ODP Leg 151). Proc., initial reports, ODP, Leg 151, North Atlantic-
1001 Arctic gateways: 1: 385-395.https://doi.org/10.2973/odp.proc.ir.151.112.1995
1002 Stranne, C., O'Regan, M., Jakobsson, M., Brüchert, V., Ketzer, M., 2019. Can anaerobic
1003 oxidation of methane prevent seafloor gas escape in a warming climate? Solid Earth,
1004 10(5): 1541-1554.https://doi.org/10.5194/se-10-1541-2019
1005 Teichert, B.M.A., Eisenhauer, A., Bohrmann, G., Haase-Schramm, A., Bock, B., Linke, P.,
1006 2003. U/Th systematics and ages of authigenic carbonates from Hydrate Ridge,
1007 Cascadia Margin: recorders of fluid flow variations. Geochimica et Cosmochimica
1008 Acta, 67(20): 3845-3857.http://dx.doi.org/10.1016/S0016-7037(03)00128-5
1009 Treude, T., Boetius, A., Knittel, K., Wallmann, K., Jørgensen, B.B., 2003. Anaerobic
1010 oxidation of methane above gas hydrates at Hydrate Ridge, NE Pacific Ocean. Marine
1011 Ecology-progress Series, 264: 1-14.https://doi.org/10.3354/meps264001
1012 Treude, T., Krause, S., Steinle, L., Burwicz, E., Hamdan, L.J., Niemann, H., Feseker, T.,
1013 Liebetrau, V., Krastel, S., Berndt, C., 2020. Biogeochemical Consequences of
1014 Nonvertical Methane Transport in Sediment Offshore Northwestern Svalbard. Journal
1015 of Geophysical Research: Biogeosciences, 125(3):
1016 e2019JG005371.https://doi.org/10.1029/2019jg005371
1017 Treude, T., Smith, C.R., Wenzhöfer, F., Carney, E., Bernardino, A.F., Hannides, A.K.,
1018 Krüger, M., Boetius, A., 2009. Biogeochemistry of a deep-sea whale fall: sulfate
1019 reduction, sulfide efflux and methanogenesis. Marine Ecology Progress Series, 382: 1-
1020 21.https://doi.org/10.3354/meps07972
1021 Vogt, P.R., Crane, K., Sundvor, E., Max, M.D., Pfirman, S.L., 1994. Methane-generated(?)
1022 pockmarks on young, thickly sedimented oceanic crust in the Arctic: Vestnesa ridge,
1023 Fram strait. Geology, 22(3): 255-258.https://doi.org/10.1130/0091-
1024 7613(1994)022<0255:Mgpoyt>2.3.Co;2
1025 Wallmann, K., Drews, M., Aloisi, G., Bohrmann, G., 2006. Methane discharge into the Black
1026 Sea and the global ocean via fluid flow through submarine mud volcanoes. Earth and
1027 Planetary Science Letters, 248(1): 545-560.https://doi.org/10.1016/j.epsl.2006.06.026

Wallmann, K., Riedel, M., Hong, W.L., Patton, H., Hubbard, A., Pape, T., Hsu, C.W., Schmidt, C., Johnson, J.E., Torres, M.E., Andreassen, K., Berndt, C., Bohrmann, G., 2018. Gas hydrate dissociation off Svalbard induced by isostatic rebound rather than global warming. Nature Communications, 9(1): 83.https://doi.org/10.1038/s41467-017-02550-9

Wegener, G., Niemann, H., Elvert, M., Hinrichs, K.U., Boetius, A., 2008. Assimilation of methane and inorganic carbon by microbial communities mediating the anaerobic oxidation of methane. Environ Microbiol, 10(9): 2287-98.https://doi.org/10.1111/j.1462-2920.2008.01653.x

Westbrook, G.K., Thatcher, K.E., Rohling, E.J., Piotrowski, A.M., Pälike, H., Osborne, A.H., Nisbet, E.G., Minshull, T.A., Lanoisellé, M., James, R.H., Hühnerbach, V., Green, D., Fisher, R.E., Crocker, A.J., Chabert, A., Bolton, C., Beszczynska-Möller, A., Berndt, C., Aquilina, A., 2009. Escape of methane gas from the seabed along the West Spitsbergen continental margin. Geophysical Research Letters, 36(15): L15608.https://doi.org/10.1029/2009GL039191

Whiticar, M.J., 1999. Carbon and hydrogen isotope systematics of bacterial formation and oxidation of methane. Chemical Geology, 161(1–3): 291-314.http://dx.doi.org/10.1016/S0009-2541(99)00092-3

Yamamoto, S., Alcauskas, J.B., Crozier, T.E., 1976. Solubility of methane in distilled water and seawater. Journal of Chemical & Engineering Data, 21(1): 78-80.https://doi.org/10.1021/je60068a029

Yao, H., Hong, W.L., Panieri, G., Sauer, S., Torres, M.E., Lehmann, M.F., Gründger, F., Niemann, H., 2019. Fracture-controlled fluid transport supports microbial methane-oxidizing communities at Vestnesa Ridge. Biogeosciences, 16(10): 2221-2232.https://doi.org/10.5194/bg-16-2221-2019

Yoshinaga, M.Y., Holler, T., Goldhammer, T., Wegener, G., Pohlman, J.W., Brunner, B., Kuypers, M.M.M., Hinrichs, K.-U., Elvert, M., 2014. Carbon isotope equilibration during sulphate-limited anaerobic oxidation of methane. Nature Geoscience, 7(3): 190-194.https://doi.org/10.1038/ngeo2069